Spotting Interface Structuring during Na-Insertion into the NaSICON Na 3 V 2 (PO 4) 3 by EQCM and Operando Fiber Optic Infrared Spectroscopy

Ezzoubair Bendadesse, Charlotte Gervillié-Mouravieff, Cédric Leau, Kateryna Goloviznina, François Rabuel, Mathieu Salanne, Jean-Marie Tarascon, Ozlem Sel

▶ **To cite this version:**

Ezzoubair Bendadesse, Charlotte Gervillié-Mouravieff, Cédric Leau, Kateryna Goloviznina, François Rabuel, et al.. Spotting Interface Structuring during Na-Insertion into the NaSICON Na 3 V 2 (PO 4) 3 by EQCM and Operando Fiber Optic Infrared Spectroscopy. Advanced Energy Materials, 2023, 13 (26), pp.2300930. 10.1002/aenm.202300930 . hal-04214161

HAL Id: hal-04214161
https://u-picardie.hal.science/hal-04214161

Submitted on 18 Jan 2024

HAL is a multi-disciplinary open access archive for the deposit and dissemination of scientific research documents, whether they are published or not. The documents may come from teaching and research institutions in France or abroad, or from public or private research centers.

L'archive ouverte pluridisciplinaire **HAL**, est destinée au dépôt et à la diffusion de documents scientifiques de niveau recherche, publiés ou non, émanant des établissements d'enseignement et de recherche français ou étrangers, des laboratoires publics ou privés.

Spotting interface structuring during Na-insertion into the NaSICON $Na_3V_2(PO_4)_3$ by EQCM and *operando* fiber optic infrared spectroscopy

Ezzoubair Bendadesse[a,b,c], Charlotte Gervillié-Mouravieff[a,c,d], Cédric Leau[a,c], Kateryna Goloviznina[c,e], François Rabuel[c,f], Mathieu Salanne[c,e,g], Jean-Marie Tarascon[a,c]* & Ozlem Sel[a,c]*

[a] Chimie du Solide et de l'Energie, UMR 8260, Collegè de France, 75231 Paris, Cedex 05, France

[b] Sorbonne Université, CNRS, Laboratoire Interfaces et Systemes Electrochimiques, LISE, UMR 8235, 75005 Paris, France

[c] Réseau sur le Stockage Electrochimique de l'Energie (RS2E), CNRS FR 3459, 80039 Amiens Cedex, France

[d] Department of NanoEngineering, University of California San Diego, La Jolla, CA, 92093, United States

[e] Sorbonne Université, CNRS, Physicochimie des Électrolytes et Nanosystemes` Interfaciaux, PHENIX, F-75005 Paris, France

[g] Institut Universitaire de France (IUF), 75231 Paris, France

[f] Université de Picardie Jules Verne, Laboratoire de Réactivité et Chimie des Solides (LRCS), UMR 7314 CNRS, HUB de l'Energie, 80039 Amiens, France

Corresponding authors:

jean.marie-tarascon@college-de-france.fr

ozlem.sel@college-de-france.fr

Keywords: Sodium ion battery, electrode/electrolyte interface, EQCM, Infrared Fiber Wave Evanescent Spectroscopy, Molecular Dynamics simulations

Abstract: Reliable operation of Na-ion batteries requires a mastering of the interfacial processes governing intercalation kinetics. Ion desolvation, amongst others, is a crucial phenomenon as far as power applications are envisioned. Studying the intricacy of interfacial processes faces experimental challenges. Here we report the complementary use of EQCM and *operando* Infrared Fiber Wave Evanescent Spectroscopy (IR-FEWS) combined with MD simulations to investigate the electrode/electrolyte interface of polyanionic Na-insertion compounds $Na_3V_2(PO_4)_3$ (NVP) and $Na_3V_2(PO_4)_2F_3$ (NVPF). Through screening of various electrolytes that differ in their solvation energy and viscosity, we demonstrate the existence of an unusual mass uptake/depletion signal at the NVP interfaces only, indicative of a dissimilarity in migration kinetics of solvent molecules between NVP and NVPF interfaces as supported by IR-FEWS. We rationalize our finding that sodium depletion is caused by the unusually rapid ion diffusion within NVP mediated by an intermediate metastable phase, which leads to opposite Na^+ concentration and free solvent molecule gradients at the interface that causes the unusual and anomalous feature observed on EQCM frequency profiles. This feature does not appear with NVPF showing lower ionic diffusion. Altogether, this fundamental study provides valuable fundamental insights on the interface structuring of insertion compounds depending upon their Na^+ mobility.

Introduction

Sodium ion batteries (SIBs) are an emerging alternative to the Li-ion technology. Their affordability coupled with a greater abundance of sodium containing precursors offer a nice trade-off in terms of cost *vs.* energy density.[1–5] Common to all alkali metal batteries, interfacial phenomena are of paramount importance. Notably, the processes governing the Electrode Electrolyte Interface (EEI) are of particular interest to the battery research community. Alike Li-ion batteries, an often unclear and elusive picture is painted when discussing interfacial phenomena in SIBs due to the limited number of non-invasive analytical techniques.[6] Moreover, amongst these phenomena is the charge transfer process leading to ion intercalation in the host structure, often evoked in discussions when it comes to high performances due to its important contribution to the kinetics of insertion.[7–9] Indeed, through past works, researchers have been able to distinguish the rate-limiting step[10–12] among the different processes constituting the charge transfer which are known to be: cation migration from the bulk of the electrolyte to the interface, desolvation, diffusion through possible interphase and finally through the bulk of the material to an electrochemically active site. However, to the best of our knowledge, no substantial correlation has been established linking the nature of the material with the processes leading to charge transfer at the interface. The solvation/desolvation process, known to be a key aspect of electrolyte engineering, was investigated using spectroscopy techniques consisting of Surface Enhanced Raman Spectroscopy (SERS)[13] or *operando* infrared spectroscopy.[14] More recently, our group reported the use of fiber optic evanescent wave sensors (FOEWS) for carrying *operando* infrared spectroscopy to unravel the dynamics of (de)solvation amongst other interface phenomena (**Scheme S1**).[15] Additionally, Electrochemical Quartz Crystal Microbalance (EQCM) based methods has become a tool of choice to quantify the solvation shell of alkali metal ions and its evolution through charge and discharge as well as to probe different salt/solvent combinations as it is illustrated in past works by our group and others.[16–20]

Herein, we examine a NaSICON material $Na_3V_2(PO_4)_3$ (NVP) to find any evidences for a close connection between the high Na^+ mobility of the NaSICON structure and the desolvation process prior to sodium intercalation. To do so, we employ EQCM, *operando* IR fibre evanescent wave spectroscopy (IR-FEWS) and MD simulations as complementary tools to investigate the dynamics of the (de)solvation process in different electrolyte solvents. More specifically, we explore the importance of electrode material/electrolyte selection on the sodium ion desolvation process and on rate capabilities of the active material targeted.

Results and Discussion

The unusual frequency variation profile of $Na_3V_2(PO_4)_3$. The NVP spray-coated quartz resonators were cycled in three different electrolytes consisting of $NaPF_6$ as a salt and PC, EC:DMC (1:1 mol) and DMC as a solvent, bearing in mind in light of our previous work that the dielectric constant is a varying parameter that affects the EQCM response of a Li^+ insertion compound.[16] **Figure 1 a-c** shows the frequency response of the NVP thin film in the three electrolytes during cyclic voltammetry between 2.8 and 3.6 V *vs.* Na/Na^+ (**Figure S1a-c**). Capacities calculated from current vs time plots were found to be 70 mAh g^{-1} and 40 mAh g^{-1} for NVP and NVPF, respectively, at a corresponding C-rate of 3C (1 mV s^{-1}). We can easily distinguish a cationic response in the form of a frequency increase/decrease during desodiation/sodiation, respectively. However, a peculiar feature of this response is the small frequency "bump" or peak that repeats upon cycling and that seems to gain in amplitude with a lower solvent polarity (from PC, EC:DMC to DMC). The peak appears exactly before the start of frequency decrease through a negative scan, which means that we have a punctual rapid mass loss followed by a mass increase due to sodiation (**Figure 1 a-c, insets**). We can speculate that we are spotting the Na ion-desolvation process, which involves the return of the solvent molecules from the coordination shells of the Na ions to the electrolyte bulk, based on the fraction of mass loss that changes inversely proportionate to the solvent polarity and viscosity. The same trend was also recorded upon inserting lithium ions into the NVP structure (**Figure S2a-c**) and during galvanostatic charge discharge *vs.* Na/Na^+ (**Figure S2d-f**). Additionally, we also observe the reverse process of ion solvation at the end of the charge/oxidation with a corresponding frequency decrease (mass gain) due to solvent molecules diffusing back to the solvent-poor interface to resolvate the Na^+ cations (**Figure S2d**). The variation of the frequency gain (caused by desolvation mass loss) as a function of the solvent's polarity is shown in **Figure S3**. For both lithium and sodium insertion, a drop in solvent polarity is associated with an increase in the % frequency gain linked to desolvation. This ties nicely with the solvation energies calculated for Na^+ bound to the carbonate solvents of interest, where weaker interactions were found linking Na^+ and linear carbonates such as DMC than cyclic carbonates such as PC and EC.[21] With weaker solvation energies, DMC molecules detach more readily than its cyclic counterpart during sodium insertion into the NVP structure, and thanks to its lower viscosity[22] it diffuses back faster to the electrolyte bulk causing the mass loss anomaly upon reduction. This further supports our belief that the brief mass loss/frequency gain peak is the result of sodium ion desolvation. For the sake of comparison, a non-NASICON polyanionic

compound in the form of $Na_3V_2(PO_4)_2F_3$ (NVPF) was then evaluated alongside with NVP (**Figure 1 d-f**).

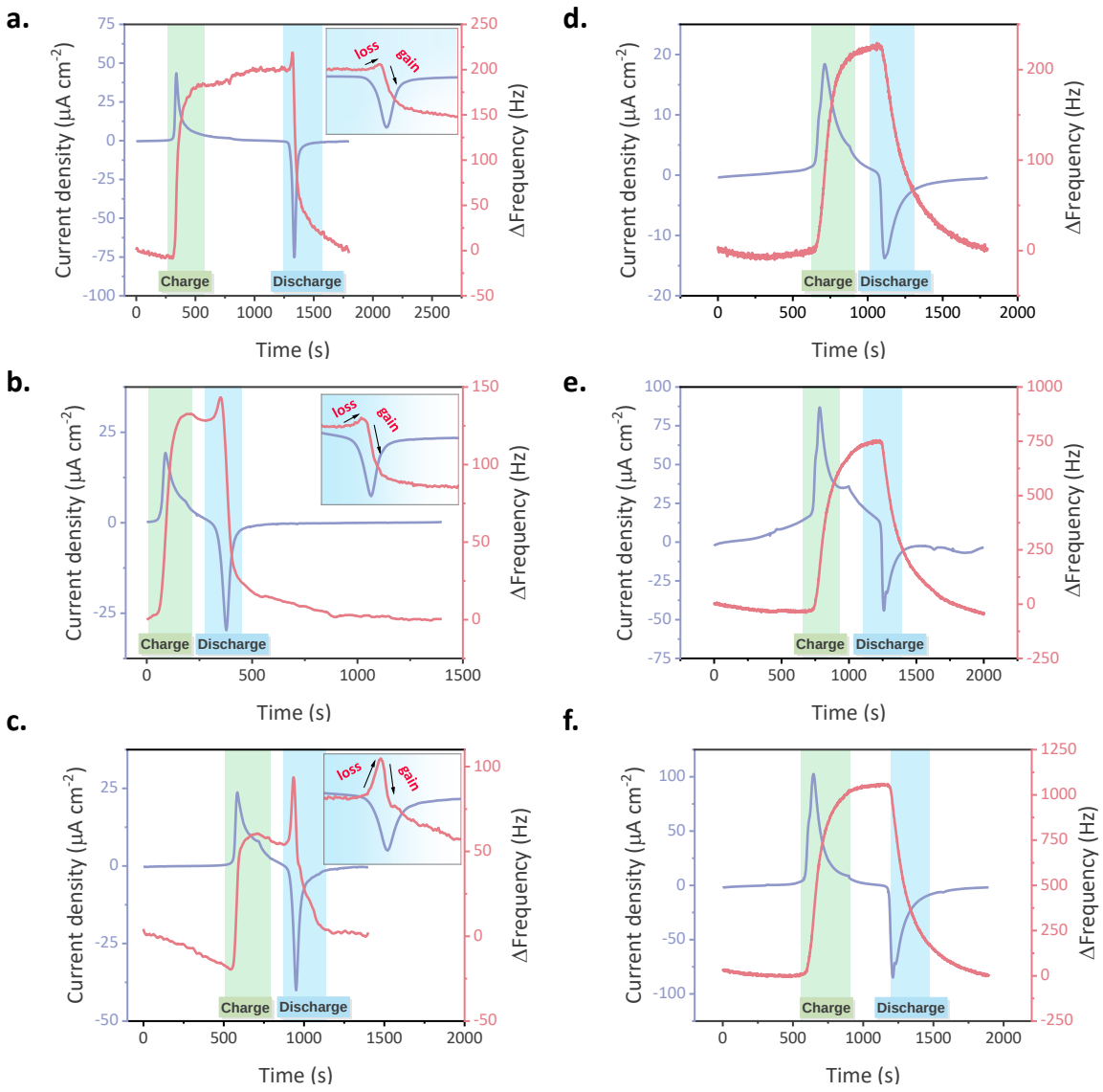

Figure 1. CV and frequency profiles of $Na_3V_2(PO_4)_3$ (NVP) **(a-c)** and $Na_3V_2(PO_4)_2F_3$ (NVPF) **(d-f)** in the three selected electrolyte: 1M $NaPF_6$ in PC, EC:DMC and DMC with 1%*vol* addition of fluoroethylene carbonate (FEC). The oxidation (charge) and the reduction (discharge) processes are portrayed with the correspondent frequency change. Inset figures in **(a-c)** are the zoom of the current versus time plots during discharge, indicating a mass loss right before the sodiation process. The 20th cycle is shown here for all experiments. All CVs were performed at 1 mV s^{-1}. Loading of the composite electrodes on the quartz resonators range from 50-80 μg cm^{-2}. Details of electrode preparation are given in Supporting Information file.

As the redox process of NVPF (de)sodiation occurs at higher potentials, we limit the charge cutoff potential to 3.9V *vs.* Na/Na^+ to prevent any electrolyte degradation from having an impact on our frequency response, especially in the DMC containing electrolytes. The EQCM response was thus recorded for the first sodium removal/intake happening at ~3.6V *vs.* Na/Na^+ (~3.35 V *vs.* Na/Na^+ for NVP) (**Figure S1 d-f**). When cycled in the same electrolytes as NVP, the NVPF thin film exhibited the expected cationic response of (de)sodiation. None of the three CV-EQCM curves showed the mass loss peak attributed to desolvation (**Figure 1 d-f**). The drastic difference in the mass variation behavior of both materials leads us to consider the influence of the materials' properties on the desolvation process. The substitution of one $(PO_4)^{3-}$ with three F^-, owing to the inductive effect, leads to an increase in the average potential of NVPF when compared to NVP and hence the energy density of the material.[23] However, it has been proven that Na^+ diffusion kinetics are faster in NVP than NVPF. For instance, Li *et al.* have shown that the NVP phase dominated the insertion kinetics at higher rates in a NVP /NVPF blended cathode.[24,25]

***Operando* IR fibre evanescent wave spectroscopy at the service of interface monitoring.** To gain further insights into the chemical origin of the punctual mass loss peak detected in EQCM analyses (**Figure 1a-c**), we ran *operando* IR fiber evanescent wave spectroscopy (IR-FEWS) measurement on the NVP system. Indeed, our group developed the possibility of applying such technique *operando* conditions using optical fibers as propagation media for IR wavelength.[15] In short, absorption spectroscopy through evanescent waves is performed at the surface of the $Te_2As_3Se_5$ (TAS) fiber that is embedded in the active material in contact with the electrolyte. The penetration depth of the evanescent waves depends on the refractive index of the surrounding media (~1 µm for the electrolytes of this study) and exceeds that of EQCM acoustic wave (range from ~140-270 nm for the electrolytes of this study). More details about the IR-FEWS setup are in the Supplementary Information file (**Scheme S1**).

NVP was cycled in two different electrolytes ($NaPF_6$ in PC and DMC 1%*vol* FEC) to highlight the difference in the dynamics of desolvation following the drastic change of solvent polarity and viscosity. Coordinated and free solvent bands were scrutinized with a special focus on the υOCO band situated between 1150 and 1400 cm^{-1} for both solvents as the solvation of Na^+ ions by DMC molecules resulted in a weakening of the νC=O vibrational band of DMC and a strengthening of the νO-C-O band (**Figures 2a** and **3a**). For clarity, only the 2nd and 3rd cycles were analyzed to avoid any electrolyte degradation related shifts of bands due to possible CEI formation. The evolution of νOCO absorbance and its relative absorbance evolution after

subtracting the reference absorbance (at t=0 when the cell was first connected) are plotted in **Figures 2b-c** and **3b-c**. The origin behind the double-plateau feature on the discharge is discussed in the Supplementary Information file (**Figure S4**).

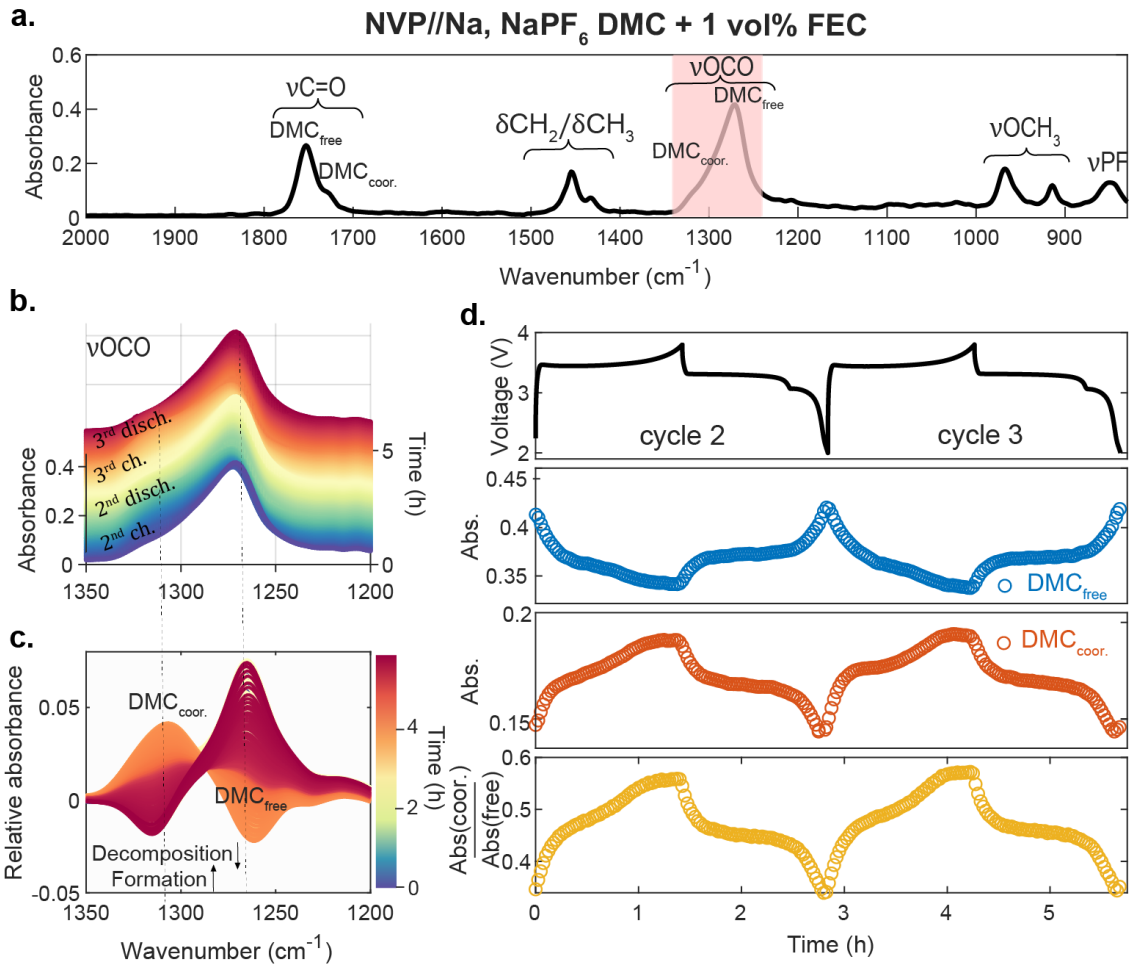

Figure 2. *Operando* IR-FEWS measurement of fiber coated and embedded in NVP with $NaPF_6$ DMC + 1*vol* % FEC electrolyte. **(a)** Absorbance IR-FEWS spectra acquired at t=0s. **(b)** Absorbance spectra in the *ν*OCO absorbance region in function of the 2nd charge (blue) 2nd discharge (green), 3rd charge (yellow) and 3rd discharge (red). **(c)** Relative variations of the absorbance spectra in the *ν*OCO absorbance region in function of the 2nd charge (blue) 2nd discharge (green), 3rd charge (yellow) and 3rd discharge (red). **(d)** Voltage evolution of the NVP/Na cells during 2nd and 3rd charge. Absorbance evolution of the *ν*OCO bands of DMC_{free} (blue), of $DMC_{coor.}$ (orange) and of the ratio of the coordinated and free bands (yellow).

The υOCO band shift during cycling was monitored in DMC (**Figure 2d**) and PC (**Figure 3d**) containing electrolytes. We can clearly notice a decrease and an increase of the band absorbance of coordinated and free solvent molecules, respectively, following discharge (*vice-versa* during charge). This evolution depicts the corresponding desolvation and solvation processes occurring during Na^+ insertion and disinsertion. The ratio of coordinated and free band absorbances is plotted versus time to portray the dynamics of the separation of sodium ions

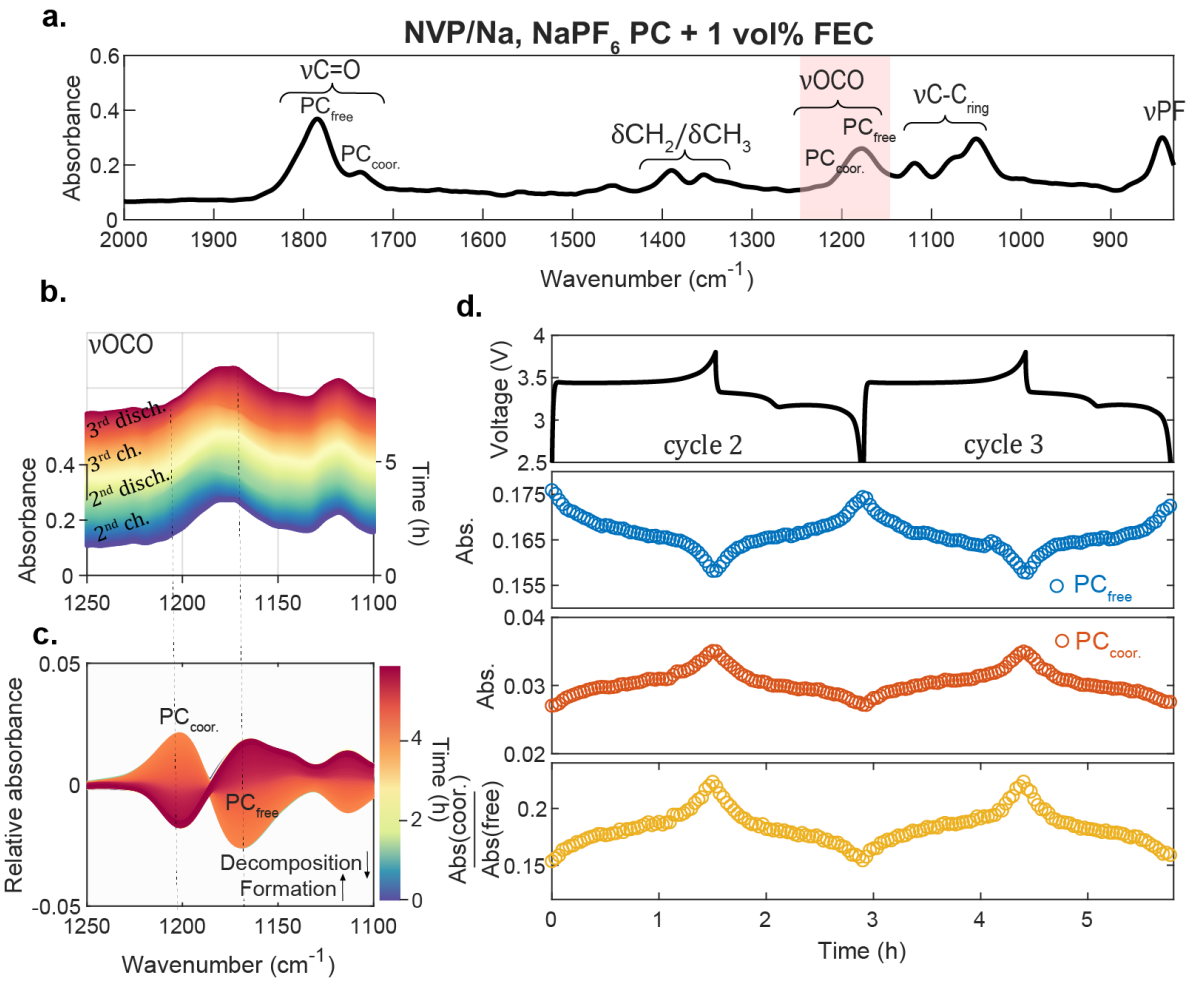

Figure 3. *Operando* IR-FEWS measurement of fiber coated and embedded in NVP with NaPF6 PC + 1 *vol*% FEC electrolyte**. (a)** Absorbance IR-FEWS spectra acquired at t= 0s. **(b)** Absorbance spectra in the νOCO absorbance region in function of the 2nd charge (blue) 2nd discharge (yellow), 3rd charge (yellow) and 3rd discharge (red). **(c)** Relative variations of the absorbance spectra in the νOCO absorbance region in function of the 2nd charge (blue) 2nd discharge (red), 3rd charge (yellow) and 3rd discharge (red). **(d)** Voltage evolution of the NVP/Na cells during 2nd and 3rd charge. Absorbance evolution of the *ν*OCO bands of PC_{free} (blue), of $PC_{coor.}$ (orange) and of the ratio of the coordinated and free bands (yellow).

from its solvation shell. A clear difference is spotted between both electrolytes as the DMC υOCO band ratio shows a rapid decay (increase) at the beginning of discharge (charge) which can be correlated to the fast depletion of free solvent molecules at the interface caused by their re-migration towards the bulk of the electrolyte upon sodium ion insertion. Meanwhile, a more linear evolution is observed in the PC electrolyte throughout both charge and discharge processes highlighting the slow diffusion of solvent molecules possibly due to higher solvent viscosity as it will be discussed later. At this stage, a legitimate question regards how such high sodium diffusion kinetics in NVP could account for the desolvation process observed by EQCM and IR-FEWS alike. While *operando* techniques are unable to replicate the exact real-life conditions of sodium-ion batteries (SIBs) operation due to equipment or technique limitations, the impact of NVP's intrinsic transport properties and the observed anomaly during the desolvation process should still be valid in actual battery conditions. This is because these processes occur at the nanoscale, suggesting that the fundamental effects would persist despite the imperfect replication of real-life conditions by *operando* techniques.

Estimating ionic the apparent diffusion coefficients. To test the aforementioned hypothesis, we estimated the apparent solid diffusion coefficient of Na^+ in both materials using two different techniques: Randles-Sevcik equation and Potentiostatic Intermittent Titration Technique (PITT) measurements (**Figure 4**) following the protocols described in Supplementary information. Both techniques were applied to thin-film configuration electrodes sprayed onto the QCM. When using Randles-Sevcik, we notice that the estimated coefficient for sodium insertion and extraction in both structures (NaSICON and non-NaSICON) are comparable, with a slightly higher value of $D_{Na}{}^+$ during discharge in NVP and charge in NVPF. **Figure 4a** and **4b** show that $D_{Na}{}^+$ values, obtained by PITT analysis for both materials are at least one order of magnitude higher than $D_{Na}{}^+$ estimated by Randles-Sevcik, this can be explained by its dynamic nature which takes into account several charge transfer steps enlisted in the Na^+ insertion process which can lead to an underestimation of the apparent diffusion coefficient. Differently, PITT analysis measures current relaxation during a potentiostatic step of a controlled duration under equilibrium conditions, thus, the estimated diffusion coefficient

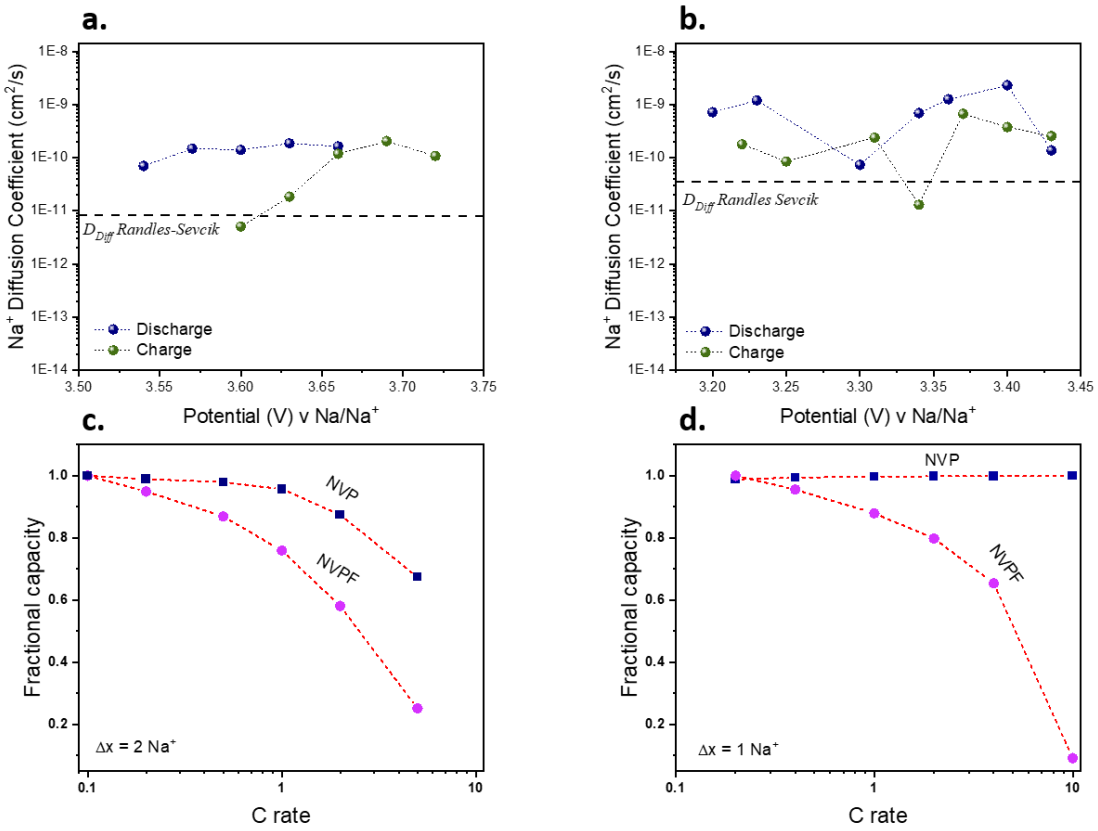

Figure 4. Apparent solid diffusion coefficients of Na^+ cations in NVPF (**a**) and NVP (**b**) estimated using PITT and Randles-Sevcik equation**.** Rate performances of NVP and NVPF with a 100% (**c**) and 50% (**d**) SOC cutoff. All experiments were conducted using a 1M $NaPF_6$ in EC:DMC + 1%vol FEC electrolyte.

should reflect the kinetics of sodium diffusion in the crystal bulk. Furthermore, the sharp drop in D_{Na^+} observed during charge and discharge in the middle of the plateau for NVP is not an experimental artefact as it has been reproduced twice, but rather due to the stronger interactions between sodium ions and host structures during the two-phase transition reaction, as previously observed for LFP and NVP.[26,27] Nonetheless, whatever the technique used, it remains that the ion diffusion in NVP (~10^{-9} cm^2 s^{-1}) is higher than in NVPF (~10^{-10} cm^2 s^{-1}), comforting our hypothesis in the influence of fast sodium diffusion ability on the structuration of the EEI.

Correlating the EQCM frequency profile anomaly to superior rate capabilities of NVP. As discussed earlier, NVP was proven to withstand high rates more efficiently than NVPF.[24,25] For a fair and direct comparison of high-rate properties between both materials, we performed power rate experiments over different rates (ranging from C/10 to 5C). We cycled both NVP and NVPF in the same electrolyte (EC:DMC 1%*vol* FEC) over the full potential windows for both materials (2-3.8V and 2-4.3V *vs.* Na/Na^+ for NVP and NVPF, respectively) (**Figure 4c**). Spectacularly, NVP fully outpaces NVPF in terms of rate performances with namely a 65% of the initial capacity retention for NVP as compared to only 20% for NPVF at 5C. Such a drastic difference in the rate performance comes somewhat as a surprise bearing in mind the one order of magnitude difference, at most, in the D_{Na^+} between both materials. To further interrogate the underlying science beyond this difference, we limit the state of charge (SOC) to its half (1 exchanged Na^+) in order to closely match the EQCM testing conditions, so as to deduce meaningful correlations if any. Surprisingly, when Δx=1 (in $Na_{3\pm x}V_2(PO_4)_3$ and $Na_{3\pm x}V_2(PO_4)_2F_3$), the NVP structure retains 100% of the initial capacity at very high rate (10C) while NVPF seems to display similar capacity fade to an unlimited SOC cutoff condition (**Figure 4d** and **Figure S5c-d**). This outstanding rate performance of NVP suggests that the first sodium ion extracted may suffers solely from minor kinetic limitations as opposed to the removal of the second Na^+. Such an observation can find its meaning in light of recent work by Chotard *et al.*[28] that demonstrated, through *operando* synchrotron X-ray diffraction (SXRD), the existence of a metastable intermediate phase during the biphasic reaction of $Na_3V_2(PO_4)_3$ – $Na_1V_2(PO_4)_3$. Indeed, $Na_2V_2(PO_4)_3$ seems to appear in a more pronounced manner during non-equilibrium conditions (high C rates) and shows a reduction in symmetry from the usual Na-poor/rich phases. This entails the splitting of Na(1) and Na(2) sites into several new positions which creates vacancies at the Na(2) sites. Additionally, due to a different connectivity to the Na(1) site that results from such site-splitting, a Na(2a) sodium site forms and may offer a faster diffusion path, explaining the cause of such high rate performances. Moreover, it was deduced that the intermediate phase considerably reduces the lattice mismatch and facilitates the Na_3-Na_1 phase transition. In contrast, the Na-driven phase transition diagram in NVPF is more complex and involves the emergence of many single phases at both SOC cutoffs (Δx=1 or 2). Besides, the fact that NVPF does not have the suited NASICON structure for fast ionic diffusion, this multiple-phase mechanism during partial and full (de)sodiation could be an additional handicap to explain the inferior rate performances of NVPF when compared to NVP.[29] At this stage a legitimate question regards the importance of this metastable phase at Δx=1 Na^+ for NVP and its effect on observed EEI structuration. Interestingly, there have been

reports mentioning the existence of a metastable phase occurring under non-equilibrium conditions[30] at Δx=0.5 Li^+ in the polyanionic $LiFePO_4$ phase. We thus explore the rate capability of $LiFePO_4$/Li half cells. **Figure S6** demonstrates that the capacity recovered at a 5C discharge rate is only half that of the initial charge capacity. This suggests that the mere presence of a metastable phase is not enough to enhance the diffusion kinetics to such outstanding levels. Besides the intricacy of phase transitions, particle size is a legitimate concern in regards to rate capabilities. Although diffusion coefficients are an intrinsic property of each material, a reduced particle size can greatly enhance power rate performances by shortening the cation travelling distance as evidenced repeatedly for an array of materials.[31,32] In our case, NVPF particles were found to be smaller than NVP particles as evidenced by SEM images (**Figure S7**), hence suggesting a higher rate performance for NVPF; the opposite of what we observed. Lastly, it should be mentioned that all materials used in this study (NVP, LFP and NVPF) were carbon coated *in-situ* via solid state synthesis to counter the inherently poor electronic conduction of polyanionic materials. Altogether, these results seem to indicate that the unusual Na^+ uptake-removal process spotted by EQCM is inherent to NASICON-type NVP and its metastable phase. Work exploring this topic is ongoing in our group.

Impact of diffusion kinetics on rate limiting step. To interrogate the effect of the enhanced diffusion kinetics on the rate-limiting step of each material, EQCM tests were conducted using CV at different sweeping rates (1 to 5 mV s^{-1}) to monitor the frequency profile during different rates. Firstly, NVPF-loaded QCM resonator seems to display lower mass exchange amplitude (smaller Δf) with higher rates (**Figure 5a-b**), meaning that the quantity of sodium intake is lower at higher rates which correlates nicely with the lower capacities obtained at higher C-rates (**Figure S5 c-d**). **Figure 5d** show the frequency variation profile for NVP, surprisingly, the amplitude increases proportionally to the sweeping rate as opposed to NVPF. Higher C-rates allow us to keep a larger portion of the initial capacity, but a capacity loss is still seen in NVP upon faster cycling (**Figure S5a**). We conclude that the desolvation process is the rate-limiting step during sodium (de)intercalation in NVP, as evidenced by the fact that the faster the sweeping rate is, the more mass appears to be transferred to the EEI (higher Δf during cathodic scan, **Figure 5d**). This suggests that the desolvation process is hampered by the fast ion transfer kinetics to the interface. More specifically, faster sweeping rates cause the concentration gradients of bare Na^+ and uncoordinated solvent molecules to develop at the interface and to become more and more prominent, increasing polarization as seen when cycling at high C-rates (**Figure S5a-b**).

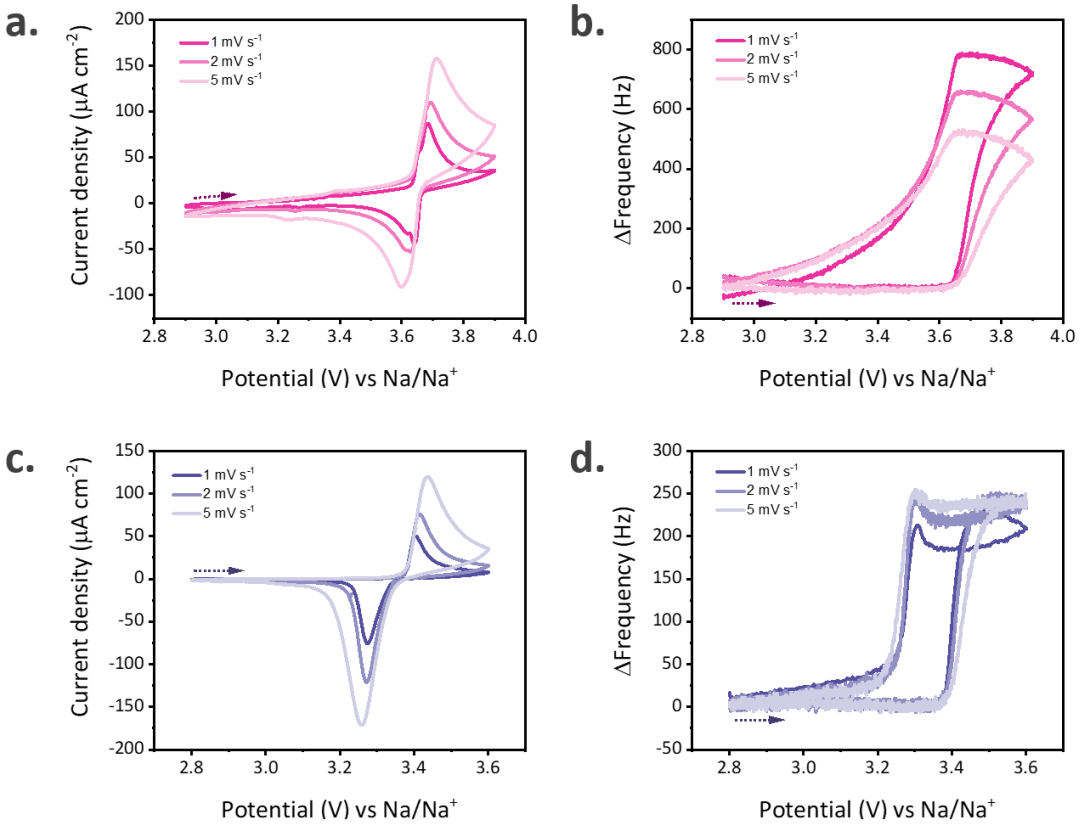

Figure 5. EQCM results where CV and frequency variation profiles performed at different sweeping rates of potential on NVPF **(a-b)** and NVP **(c-d)** loaded QCM resonators in 1M $NaPF_6$ in EC:DMC + 1%*vol* FEC. The arrows shows the scan direction.

Confirmation of the desolvation by MD simulations. In order to rationalize these experimental findings, we performed MD simulations of the 1 M $NaPF_6$ in PC in the contact with the NVP electrode. In equilibrium condition, with no voltage applied, the closest layer is formed by PC molecules (**Figure 6a**) adopting two different orientation of carbonyl groups with respect to the electrode surface (the peaks at ~3.1 Å and ~5.9 Å). The second solvent layer includes not only the PC molecules (broad low-intense peak at ~8.6 Å) but also the $NaPF_6$ salt (peaks at 9.2 Å and 9.4 Å for Na^+ and P of PF_6^-, respectively), as is illustrated by the simulation snapshot (**Figure 6b**). Such a structural arrangement in the equilibrium state creates a prerequisite for the formation of the concentration gradient during the interaction of the Na^+ ions into the NVP. The second effect traceable by MD simulations is the desolvation of sodium ions. In the bulk, a single Na^+ cation is surrounded by ~0.95 anions and ~4.75 solvent molecules, on average, in its first coordination shell (**Figure S10b**). On the contrary, while

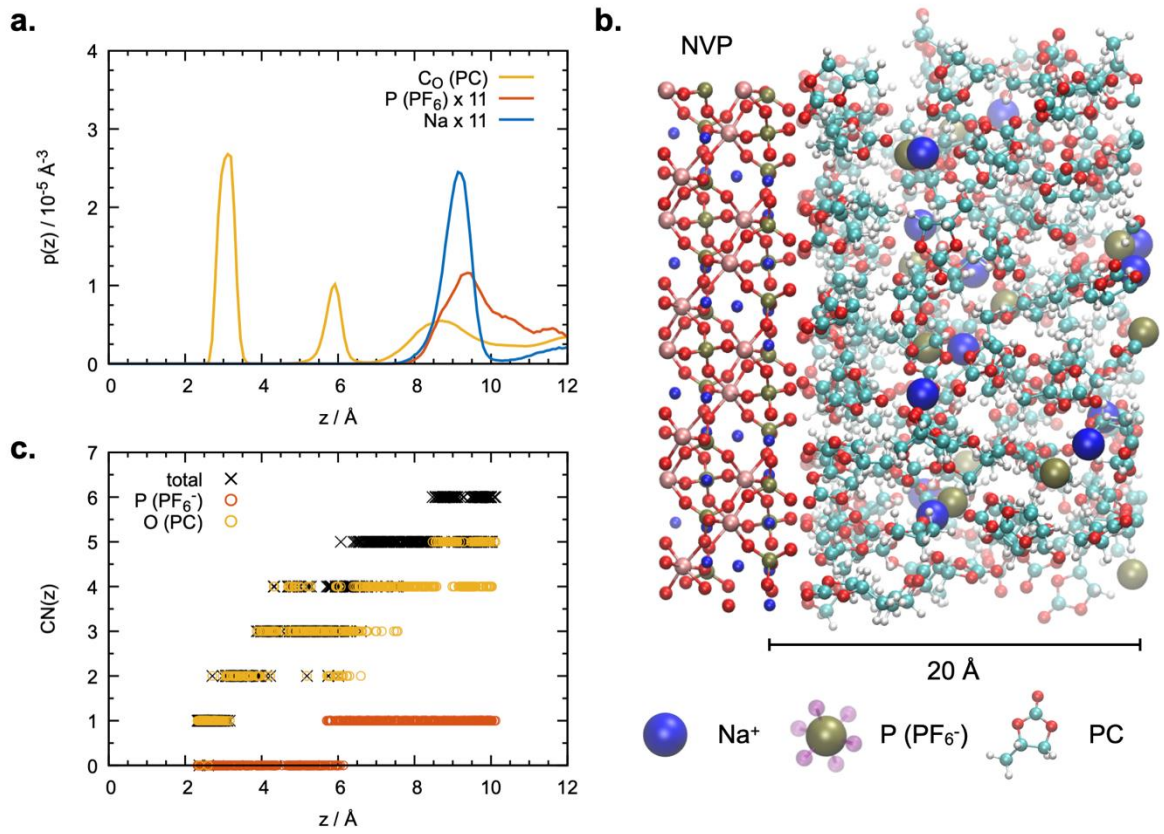

Figure 6. MD simulations of an equilibrium NVP//Na/$NaPF_6$ PC system with no voltage applied. (**a**) Density profiles of the Na^+ cations, P atom of the PF_6^- anions and C atom of the carbonate group of PC as a function of the distance from NVP electrode. The intensities of Na and P are multiplied by the molar ratio of PC/$NaPF_6$ ≃ 11. Top Na layer of the NVP electrode is considered as z = 0 Å. (**b**) Simulation snapshot of the NVP//Na/$NaPF_6$ PC system. (**c**) Coordination number (CN) of P atom of the PF_6^- anions and O atom of the carbonyl group of PC around the Na^+ cation as the function of the distance of Na^+ to the NVP surface. The cutoff values for the first coordination shell of Na^+ are 4.55 Å for P and 3.20 Å for O atoms. Each symbol corresponds to a separate snapshot of a trajectory during which a single Na^+ cation was pulled from the bulk to the NVP surface.

approaching the NVP surface, its total coordination number continuously decreases from *six* at about 9-10 Å from the surface to *one* at about 2-3 Å (**Figure 6c**). The sodium ion is not able to preserve its solvation shell when diffusing through the dense solvent layer at the surface since an important energy barrier should be overcome. Therefore, the experimental findings are confirmed by the simulations.

Conclusion

We believe that thanks to the high sodium ion mobility in the bulk of NVP and the presence of the metastable intermediate phase upon sodium insertion, there is a depletion of bare (desolvated) Na^+ at close surface, creating a concentration gradient at the interface, which in turn induces an opposite concentration gradient of uncoordinated solvent molecules. This will drive the latter to diffuse back to the bulk of the electrolyte and thus be detected by the QCM resonator as a mass loss. As for the case of NVPF, the uncoordinated solvent molecules do not diffuse as far away from the interface as in NVP's case. The whole desolvation and diffusion process is fully confined within the penetration depth of the acoustic wave emanating from the QCM resonator and thus remains undetectable. The penetration depth, δ_n, is calculated to be 271, 198, 140 nm for PC, EC:DMC and DMC, respectively.[33]

Such a scenario can be pictured via a qualitative model (**Scheme 1**) where opposing concentration gradients coexist at the interface are sketched together with the penetration depth variation superimposed. This explains how it is feasible to observe the mass loss from desolvating Na^+ cations before they are inserted into the NaSICON material. Moreover, the mass loss could potentially be attributed in part to the anions participating the charge shielding of the electrode's surface upon polarization and the resulting Electrical Double Layer (EDL). But, this possibility is discarded as we have demonstrated in our recent work that anions populating the EDL were ejected during lithiation of Li_xMoO_3 in a PC containing electrolyte but became less mobile when DMC was used as a solvent due to contact ion pair and aggregate formation.[16] Here, because of the pronounced concentration gradient at the interface and the lower viscosity of such a linear carbonate solvent,[22] free DMC molecules diffuse more quickly than PC molecules during cycling. This is in accordance with the IR-FEWS results that show a clear difference in solvent diffusion kinetics based on polarity and viscosity (**Figure 2** and **3**), similar to the distinction between the two electrolytes' EQCM profiles, where we see a much more pronounced desolvation "peak" in DMC than in PC (**Figure 1a-c** and **Figure S3**). This is further confirmed by the MD simulations at equilibrium where a similar structuration of solvent molecules and cations is observed (**Figure 6**).

Based on these findings, one can strategize different approaches to deal with the shortcomings of each material by a careful selection of electrolyte/electrode combination. For instance, "soft-solvating" electrolytes, as proposed by Wang et al[34], could be considered to overcome the rate-limiting desolvation process in NVP's case and lower the concentration-driven polarization. On

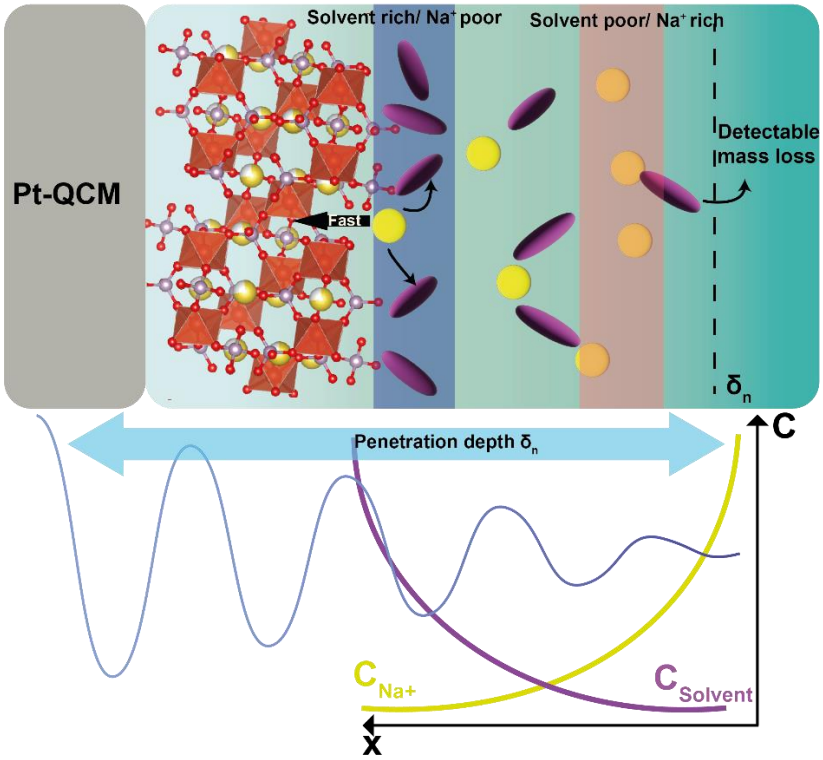

Scheme 1. Scheme representing the model of opposing concentration gradient accentuated by the fast intercalation kinetics of the host NVP framework during reduction. The penetration depth of the acoustic wave emanating from the resonator is superimposed.

the other hand, NVPF would benefit from a more stable CEI to prevent capacity fade related to vanadium dissolution[35] issues by incorporating electrolytes that would favor the formation of an inorganic CEI such as Localized High Concentration Electrolytes (LHCE).[36,37]

In conclusion, the desolvation process during the insertion of Na^+ in the NVP framework was captured thanks to EQCM and *operando* infrared spectroscopy measurements and confirmed by MD simulations. We infer that the origin behind the appearance of such punctual phenomenon is the high Na^+ diffusion kinetics properties of the NaSICON structured $Na_3V_2(PO_4)_3$ as the desolvation process creates opposing solvent and bare Na^+ concentration gradient, leading the solvent molecules to migrate in the opposite direction out of the probed boundary of the QCM resonator. As a comparison, NVPF, shown to have slower bulk diffusion kinetics, does not exhibit the mass loss peak attributed to desolvation from which we conclude that desolvation is confined within the penetration depth of the resonator's acoustic wave and becomes undetectable for classical EQCM measurements. Altogether, these findings provide a

clearer picture of the sodium-ion interface structuring in polyanionic compounds that should enable to design better electrode/electrolyte combinations to enhance SIBs performances.

Associated Content

Experimental details of thin film elaboration ($Na_3V_2(PO_4)_3$, $Na_3V_2(PO_4)_2F_3$ and $LiFePO_4$) on quartz resonators, electrochemical and EQCM analyses, estimation of apparent solid diffusion coefficient of Na^+ by PITT and Randles-Sevcik and the *operando* IR-FEWS spectroscopy procedure, the MD simulation protocol and the force field details.

Conflict of Interest

The authors declare no conflict of interest.

Acknowledgements

EB, OS and JMT acknowledge the "Sorbonne Université - Programme doctoral Génie des Procédés" for the PhD scholarship. OS and JMT also acknowledge the funding from DIM-RESPORE. KG and MS acknowledge the funding from European Research Council (ERC) under the European Union's Horizon 2020 research and innovation program (grant agreement 771294). Computational tasks were performed using resources from GENCI-IDRIS (grant 2022-A0120910463) and from the MeSU supercomputer of the Sorbonne University.

References

[1] N. Yabuuchi, K. Kubota, M. Dahbi, S. Komaba, *Chem. Rev.* **2014**, *114*, 11636.
[2] C. Vaalma, D. Buchholz, M. Weil, S. Passerini, *Nat. Rev. Mater.* **2018**, *3*, 1.
[3] J.-Y. Hwang, S.-T. Myung, Y.-K. Sun, *Chem. Soc. Rev.* **2017**, *46*, 3529.
[4] K. Chayambuka, G. Mulder, D. L. Danilov, P. H. L. Notten, *Adv. Energy Mater.* **2018**, *8*, 1800079.
[5] H. Hijazi, P. Desai, S. Mariyappan, *Batter. Supercaps* **2021**, *4*, 881.
[6] D. Kurouski, M. Mattei, R. P. Van Duyne, *Nano Lett.* **2015**, *15*, 7956.
[7] Y. Liu, Y. Zhu, Y. Cui, *Nat. Energy* **2019**, *4*, 540.
[8] Y. Zheng, T. Zhou, C. Zhang, J. Mao, H. Liu, Z. Guo, *Angew. Chem.* **2016**, *128*, 3469.
[9] M. Weiss, R. Ruess, J. Kasnatscheew, Y. Levartovsky, N. R. Levy, P. Minnmann, L. Stolz, T. Waldmann, M. Wohlfahrt-Mehrens, D. Aurbach, M. Winter, Y. Ein-Eli, J. Janek, *Adv. Energy Mater.* **2021**, *11*, 2101126.
[10] Y. Tang, Y. Zhang, W. Li, B. Ma, X. Chen, *Chem. Soc. Rev.* **2015**, *44*, 5926.

[11] X. Zhang, Z. Ju, Y. Zhu, K. J. Takeuchi, E. S. Takeuchi, A. C. Marschilok, G. Yu, *Adv. Energy Mater.* **2021**, *11*, 2000808.
[12] K. Xu, A. von Cresce, U. Lee, *Langmuir* **2010**, *26*, 11538.
[13] G. Yang, I. N. Ivanov, R. E. Ruther, R. L. Sacci, V. Subjakova, D. T. Hallinan, J. Nanda, *ACS Nano* **2018**, *12*, 10159.
[14] C. Marino, A. Boulaoued, J. Fullenwarth, D. Maurin, N. Louvain, J.-L. Bantignies, L. Stievano, L. Monconduit, *J. Phys. Chem. C* **2017**, *121*, 26598.
[15] C. Gervillié-Mouravieff, C. Boussard-Plédel, J. Huang, C. Leau, L. A. Blanquer, M. B. Yahia, M.-L. Doublet, S. T. Boles, X. H. Zhang, J. L. Adam, J.-M. Tarascon, *Nat. Energy* **2022**, 1.
[16] E. Bendadesse, A. V. Morozov, A. M. Abakumov, H. Perrot, J.-M. Tarascon, O. Sel, *ACS Nano* **2022**.
[17] P. Lemaire, A. Serva, M. Salanne, G. Rousse, H. Perrot, O. Sel, J.-M. Tarascon, *ACS Appl. Mater. Interfaces* **2022**, *14*, 20835.
[18] P. Kitz, M. Lacey, P. Novák, E. Berg, *J. Power Sources* **2020**, *477*, 228567.
[19] A. Nimkar, F. Malchick, B. Gavriel, M. Turgeman, G. Bergman, T. Fan, S. Bublil, R. Cohen, M. Weitman, N. Shpigel, *ACS Energy Lett.* **2021**, *6*, 2638.
[20] V. Dargel, N. Shpigel, S. Sigalov, P. Nayak, M. D. Levi, L. Daikhin, D. Aurbach, *Nat. Commun.* **2017**, *8*, 1389.
[21] M. Shakourian-Fard, G. Kamath, K. Smith, H. Xiong, S. K. R. S. Sankaranarayanan, *J. Phys. Chem. C* **2015**, *119*, 22747.
[22] R. Naejus, D. Lemordant, R. Coudert, P. Willmann, *J. Chem. Thermodyn.* **1997**, *29*, 1503.
[23] S. Chu, S. Guo, H. Zhou, *Chem. Soc. Rev.* **2021**, *50*, 13189.
[24] Z. Yang, G. Li, J. Sun, L. Xie, Y. Jiang, Y. Huang, S. Chen, *Energy Storage Mater.* **2020**, *25*, 724.
[25] J. Cheng, Y. Chen, S. Sun, Z. Tian, Y. Linghu, Z. Tian, C. Wang, Z. He, L. Guo, *Ceram. Int.* **2021**, *47*, 18065.
[26] Q. Wang, B. Zhao, S. Zhang, X. Gao, C. Deng, *J. Mater. Chem. A* **2015**, *3*, 7732.
[27] K. Tang, X. Yu, J. Sun, H. Li, X. Huang, *Electrochimica Acta* **2011**, *56*, 4869.
[28] S. Park, Z. Wang, Z. Deng, I. Moog, P. Canepa, F. Fauth, D. Carlier, L. Croguennec, C. Masquelier, J.-N. Chotard, *Chem. Mater.* **2022**, *34*, 451.
[29] Q. Liu, D. Wang, X. Yang, N. Chen, C. Wang, X. Bie, Y. Wei, G. Chen, F. Du, *J. Mater. Chem. A* **2015**, *3*, 21478.
[30] Y. Orikasa, T. Maeda, Y. Koyama, H. Murayama, K. Fukuda, H. Tanida, H. Arai, E. Matsubara, Y. Uchimoto, Z. Ogumi, *J. Am. Chem. Soc.* **2013**, *135*, 5497.
[31] N.-H. Kwon, T. Drezen, I. Exnar, I. Teerlinck, M. Isono, M. Graetzel, *Electrochem. Solid-State Lett.* **2006**, *9*, A277.
[32] J. Li, C. Daniel, D. Wood, *J. Power Sources* **2011**, *196*, 2452.
[33] M. D. Levi, N. Shpigel, S. Sigalov, V. Dargel, L. Daikhin, D. Aurbach, *Electrochimica Acta* **2017**, *232*, 271.
[34] J. Xu, J. Zhang, T. P. Pollard, Q. Li, S. Tan, S. Hou, H. Wan, F. Chen, H. He, E. Hu, K. Xu, X.-Q. Yang, O. Borodin, C. Wang, *Nature* **2023**, *614*, 694.
[35] P. Desai, J. Forero-Saboya, V. Meunier, G. Rousse, M. Deschamps, A. M. Abakumov, J.-M. Tarascon, S. Mariyappan, *Energy Storage Mater.* **2023**, *57*, 102.
[36] J. Zheng, S. Chen, W. Zhao, J. Song, M. H. Engelhard, J.-G. Zhang, *ACS Energy Lett.* **2018**, *3*, 315.
[37] Y. Wang, R. Jiang, Y. Liu, H. Zheng, W. Fang, X. Liang, Y. Sun, R. Zhou, H. Xiang, *ACS Appl. Energy Mater.* **2021**, *4*, 7376.

Supporting information file for

Spotting interface structuring during Na-insertion into the NaSICON $Na_3V_2(PO_4)_3$ by EQCM and *operando* fiber optic infrared spectroscopy

Table of contents

Part I. Experimental Section

Electrode preparation: Active materials $Na_3V_2(PO_4)_3$ (NVP), $Na_3V_2(PO_4)_2F_3$ (NVPF) (Tiamat) and $LiFePO_4$ (LFP) (Umicore) were used as received. The powders were mixed with carbon super P (Csp) and Poly(vinylidene fluoride-co-hexafluoropropylene) (PVDF-HFP) (80:10:10 in weight %) and grinded using a mortar and pestle, n-methyl-2-pyrrolidone (NMP) was then added drop by drop until the desired consistency was achieved. The slurry was then casted onto an aluminum sheet using a doctor blade. The casted film was dried at 120°C in air overnight to allow solvent evaporation, 12.7mm electrodes were then punched and subsequently dried at 80°C in a vacuum oven overnight. The loading was kept at 2-3 mg cm^{-2}.

Electrochemical and electrogravimetric characterization: A diluted slurry using NMP as a solvent (72:18:12 active material:Csp:PVDF *wt%*) was first prepared and sonicated to ensure homogenous particle dispersion. The platinum-patterned 9MHz QCM resonators (Bio-Logic) were heated at 150°C during the spraying process to evaporate the solvent upon contact and were heated at 200°C during 30 minutes to melt the binder and ensure good film cohesion. The resonators modified with the $Na_3V_2(PO_4)_3$ (NVP) and $Na_3V_2(PO_4)_2F_3$ (NVPF) thin films were mounted in an airtight EQCM cell developed in our previous work.[1] The cell is mounted in an Ar-filled glove-box and the measurements were conducted outside the glove-box. The EQCM with motional resistance monitoring (EQCM-R) was performed using a Biologic SP200

workstation coupled with a commercial SEIKO QCM922A microbalance which permitted the resonance frequency (*f*) along with the motional resistance (R_m) to be monitored during electrochemical cycling. Coated QCMs act as working electrode and metallic sodium acts as both reference and counter electrodes. The electrolyte concentration (1 mol L^{-1}) was kept constant, using sodium hexafluorophosphate ($NaPF_6$) in combination with 3 different solvents (propylene carbonate (PC), ethylene carbonate:dimethyl carbonate (EC:DMC) (1:1 mol) and dimethyl carbonate (DMC)) 1%*vol* addition of fluoroethylene carbonate (FEC). The cell was cycled using cycling voltammetry (CV) or galvanostatic cycling with potential limitation (GCPL) and the frequency response of the coated QCM resonator was simultaneously monitored. The EQCM tests of NVP were also performed in 1M $LiPF_6$ in DMC, EC:DMC and PC, for comparison purposes.

IR fibre evanescent wave spectroscopy (IR-FEWS): A 19 mm-diameter Swagelok cell's body was drilled from side to side, and the electrode slurry was applied using a stainless steel current collector (**Figure S1a**). The holes in the cell body were lined up with the positions of the stainless steel plunger and current collector so that the fiber could pass through the hole above the current collector. The fiber was once connected to the spectrometer to gather background information after being fixed on both sides with cured epoxy for 12 hours. The surface of the fiber and the current collector were then covered with a droplet of the electrode formulation. Finally, the entire assembly was dried in a vacuum oven overnight at 80 °C. The cells were put together in a glove box using two glass fiber separators (GF/D, Whatman) and a disc of sodium metal.

The *operando* measurements were performed with a Fourier-transformed infrared spectrometer (T37 or Invenio S, Bruker) with an accessory connection system on the right side to focus the infrared beam on one entry extremity of the fibre. The optical signal at the output extremity of the fiber was recorded using a mercury-cadmium-tellurium detector with a spectral range of 12,000-600 cm^{-1}. Liquid nitrogen was used to chill the mercury-cadmium-tellurium detector throughout each experiment. The TAS fiber's edges were manually cut for each experiment. The edge had to be flat, perpendicular and clean to have the beam going through the fibre with minimal loss. Then, using a bare fibre terminator and multimode connectors, the fibres were attached to the light source and the detector. The signal between the input and output of the fibre was controlled, with an amplitude around 10,000 for 150 µm TAS fibre. The IR-FEWS spectra were acquired with 16 scans and a resolution of 4 cm^{-1} for a total acquisition time of 4 seconds. The spectra were recorded every 30 seconds during all the electrochemical tests.

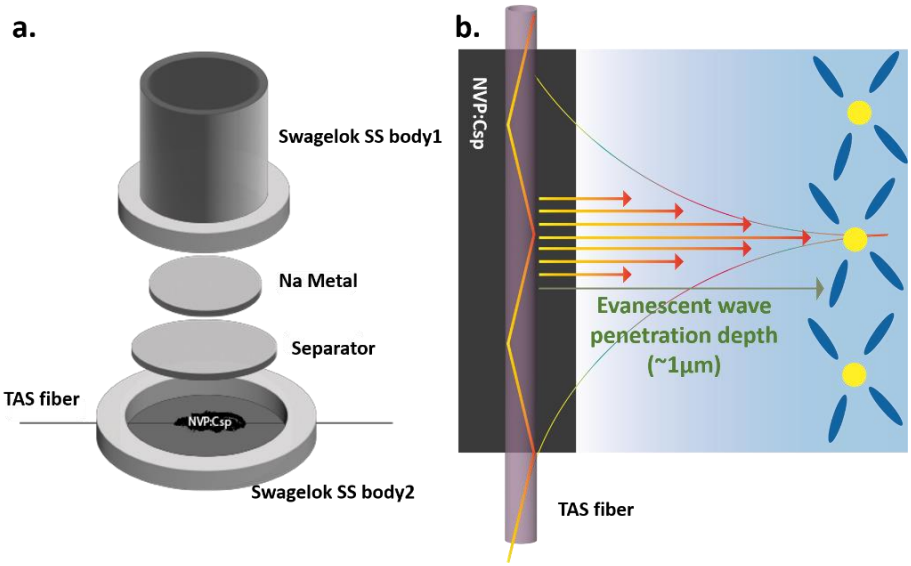

Scheme S1. *Operando* IR spectroscopy setup description scheme, the TAS fibre is embedded into a composite powder electrode of NVP:Csp (80:20 %*wt*) **(a)**. Focus on the fiber/electrode-electrolyte interface **(b)**. The evanescent wave's penetration depth represents the range at which chemical identification of species of interest is possible using this type of setup.

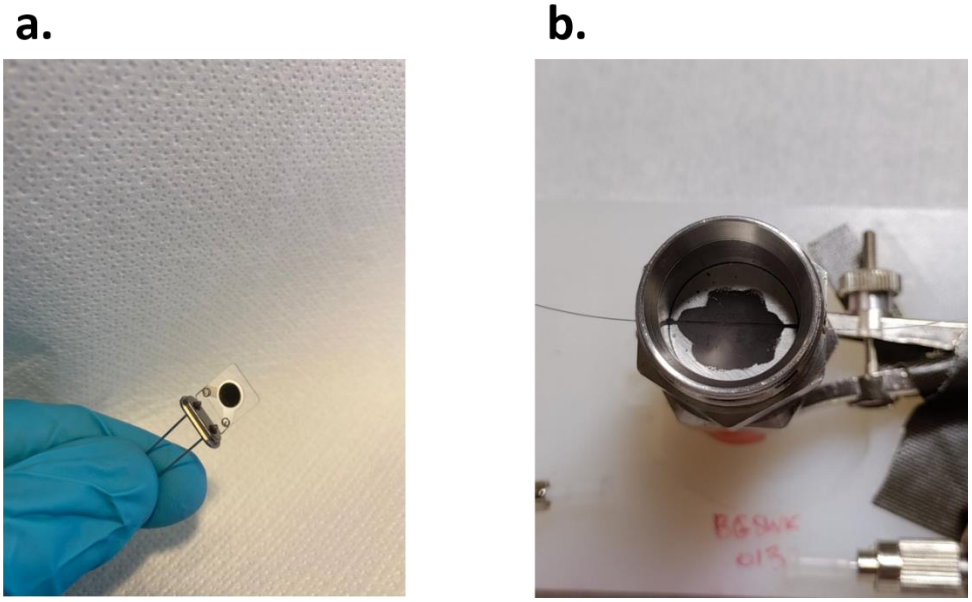

Scheme S2. Pictures of the electrodes used for **a)** EQCM measurements and **b)** IR-FEWS measurements.

The loading of the electrodes was 50-80 µg cm^{-2} and 10 mg cm^{-2} for EQCM and IR-FEWS setups, respectively. The thickness estimated from the tap densities of both NVP and NVPF at similar particle size would be as follow: 400-600 nm for the EQCM thin film and ~60 µm for the drop-cast IR-FEWS electrode. The amount of active material utilized estimated from experimental and theoretical capacities would be 56% for NVP and 66% for NVPF.

Part II. EQCM analysis of NVP

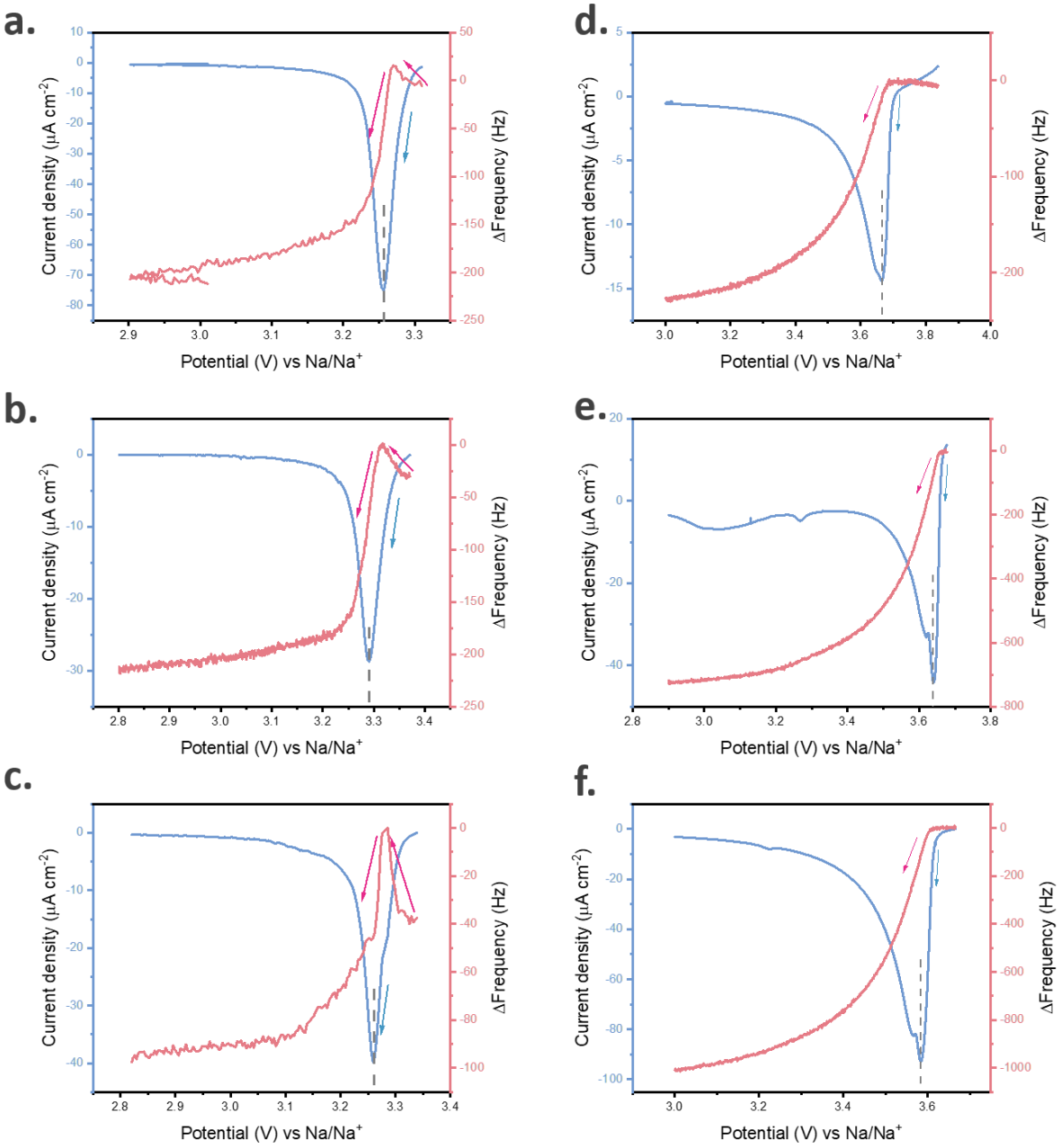

Figure S1. A zoom-in on the reduction process (sodiation) with its corresponding frequency variation profile obtained during CV: for NVP **(a-c)** cycled in 1M $NaPF_6$ in PC **(a)**, EC:DMC **(b)** and DMC **(c)** and for NVPF **(d-f)** cycled in 1M $NaPF_6$ in PC **(d)**, EC:DMC **(e)** and DMC **(f)**. All CV measurements were performed at 1 mV s^{-1}. The 20^{th} cycle is shown here for all experiments.

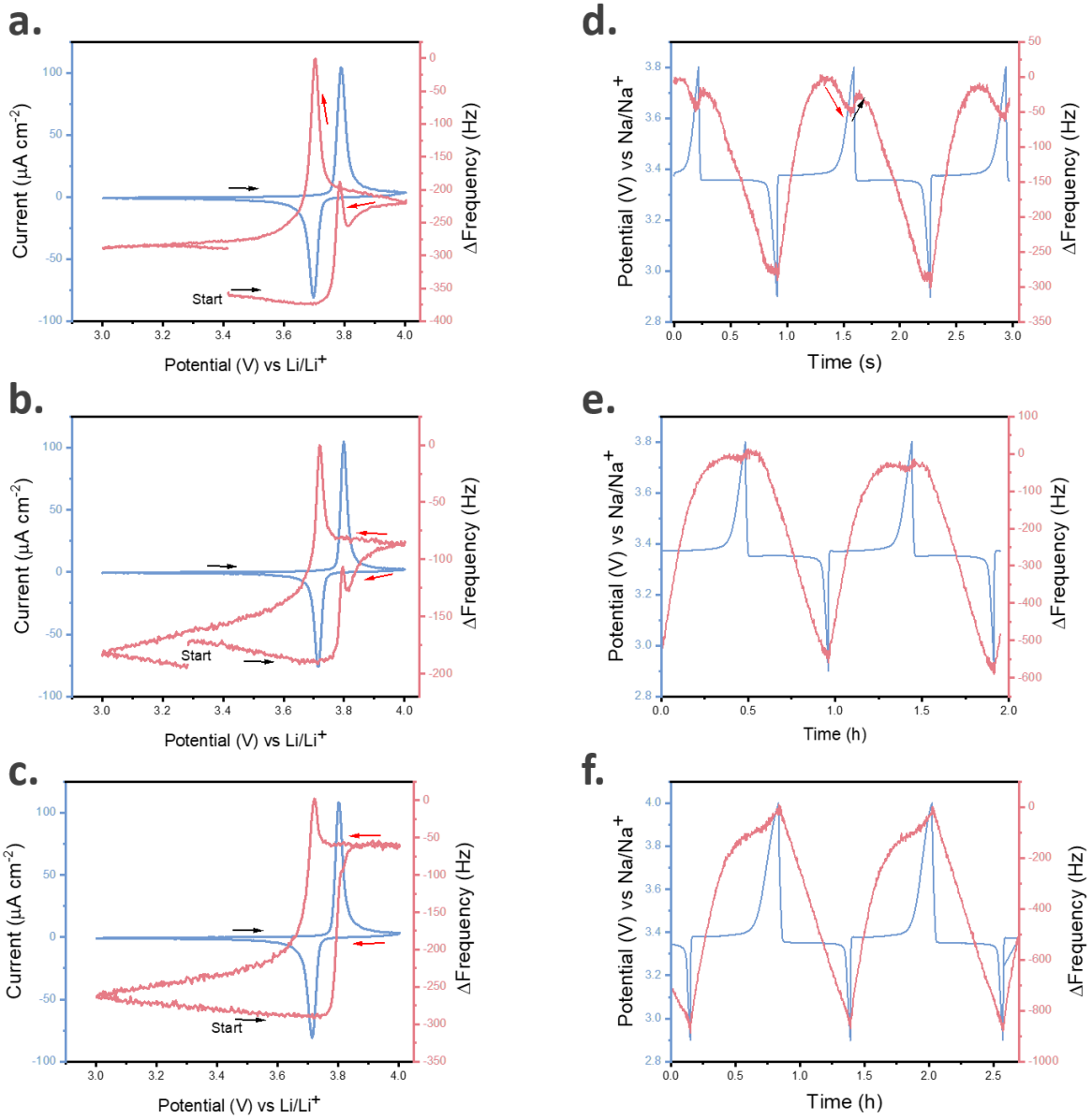

Figure S2. CV-frequency profiles of NVP loaded resonators cycled in 1M $LiPF_6$ in DMC, EC:DMC and PC (left to right, respectively **(a-c)** and GCPL profiles of NVP loaded resonators cycled in 1M $NaPF_6$ in DMC, EC:DMC and PC (left to right, respectively) **(d-f)**, experiments were conducted at $1mV.s^{-1}$ **(a-c)** and at 1C rate **(d-f)**, 5^{th} cycle is shown for all experiments.

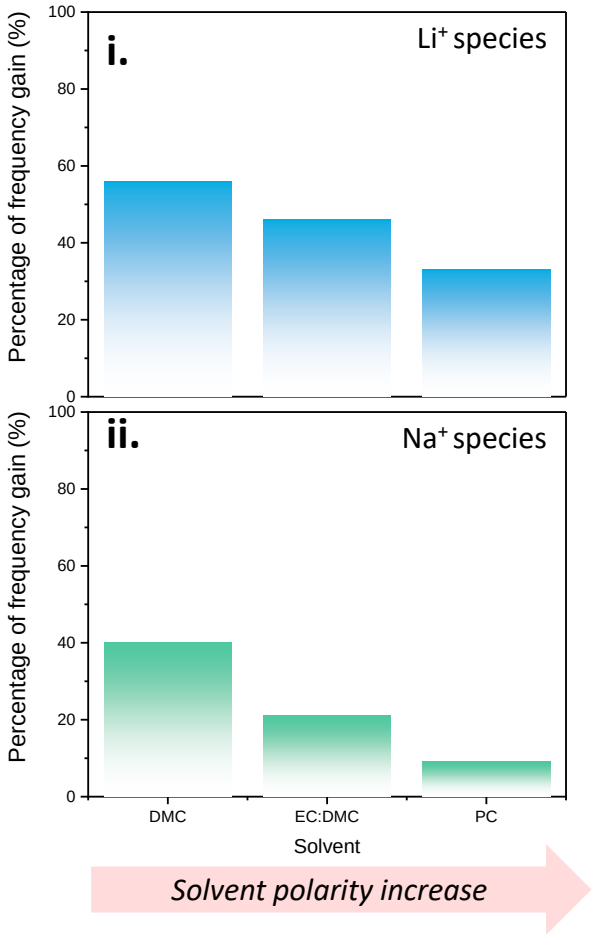

Figure S3. Evolution of the % frequency gain (relative to the full amplitude variation) caused by desolvation mass loss following the polarity of our selected solvents. i) in 1M $LiPF_6$ in DMC, EC:DMC (1:1 mol) and PC and ii) in 1M $NaPF_6$ in DMC, EC:DMC (1:1 mol) and PC.

Part III. Origin of two-plateau behavior in the IR-FEWS measurements

The double plateau observed on the discharge curve of the IR-FEWS cycling data can find its explanation in a study conducted by our group where the effect of FEC as an additive is investigated on Na metal.[2] Indeed, it has been concluded that the sodium metal's reactivity towards FEC caused the apparition of a second plateau upon discharge. The second plateau was hypothesized to be caused by sodium plating on the protective SEI layer on sodium metal formed by FEC degradation. To put it more clearly, upon cathode sodiation (discharge) the "fresh" sodium metal plated on the SEI is stripped and once depleted, the bulk sodium metal is stripped instead which causes a sudden drop in cell voltage observed in our IR-FEWS cycling curve.

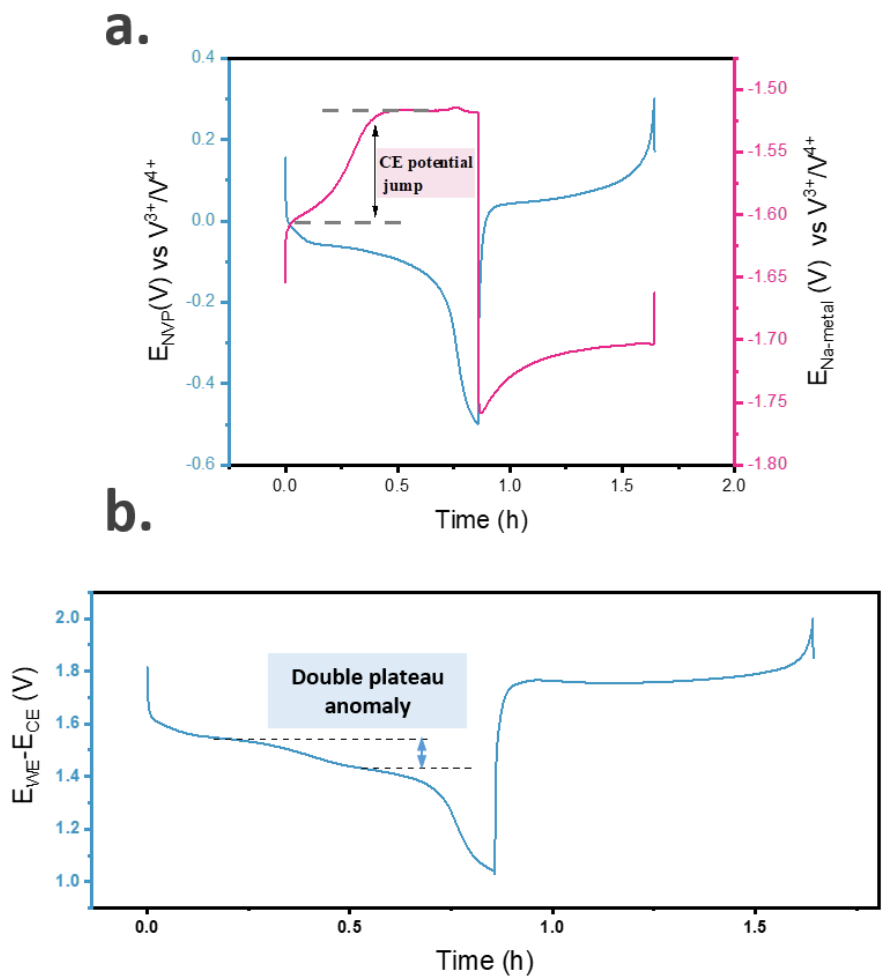

Figure S4. Three electrodes cell cycling data, comprising of NVP:Csp powder (80:20 %*wt*) as a working electrode, sodium metal as a counter and half charged NVP as a reference electrodes. **(a)** Potential profile during discharge and charge of NVP and sodium metal and **(b)** cell voltage profile during the same discharge and charge cycle showcasing the FEC-sodium metal related anomaly.

To confirm that it is indeed a Na-metal artefact, we conducted a 3-electrode experiment to separate both working electrode (NVP) and counter electrode (Sodium metal) potentials. Half charged NVP was used as a reference with a stable voltage of 3.375 V vs Na/Na^+ corresponding to the V^{3+}/V^{4+} redox couple of NVP. **Figure S4a** shows that indeed upon NVP sodiation (discharge) the sodium metal potential jumps around 100 mV causing a distinct double plateau behavior on the cell voltage (E_{WE}-E_{CE}) (**Figure S4b**).

Part IV. Charge/discharge profile of NVP, NVPF and LFP

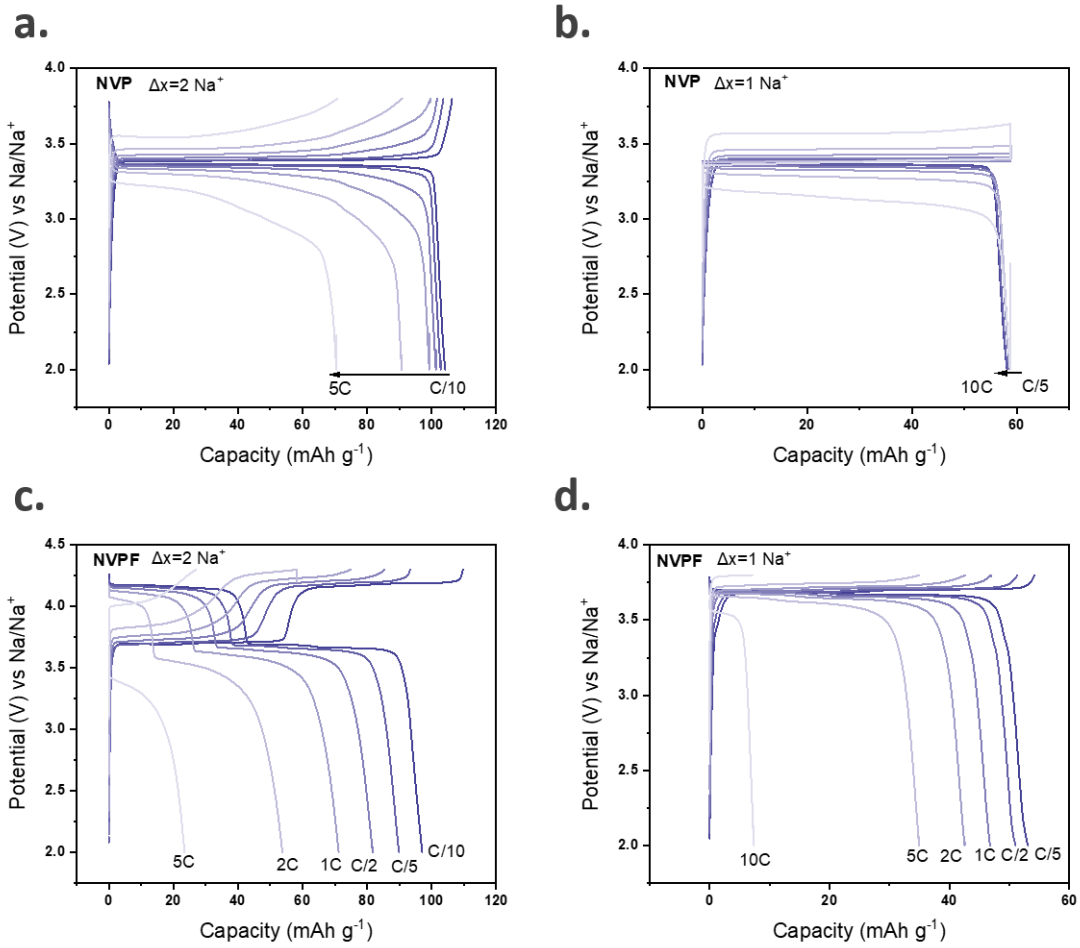

Figure S5. Charge/Discharge profile of NVP **(a,b)** and NVPF **(c,d)** cycled under two different SOC cutoffs: 100% **(a,c)** and 50% **(b,d)**.

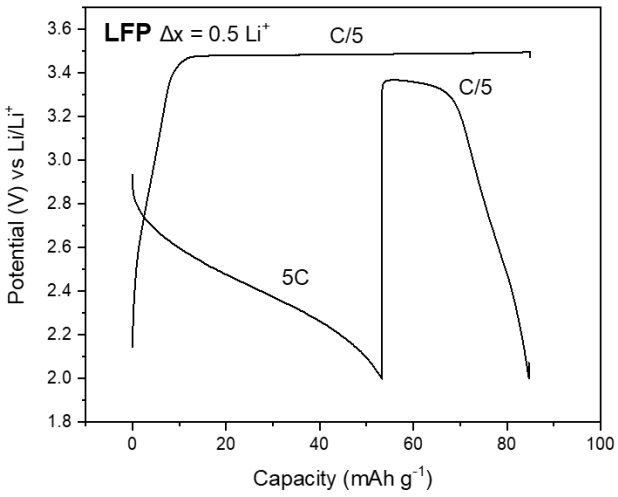

Figure S6. Charge/discharge profile of $LiFePO_4$ (LFP) at limited SOC cutoff (50%). Charge was performed at slow rate C/5 followed by fast discharge (5C).

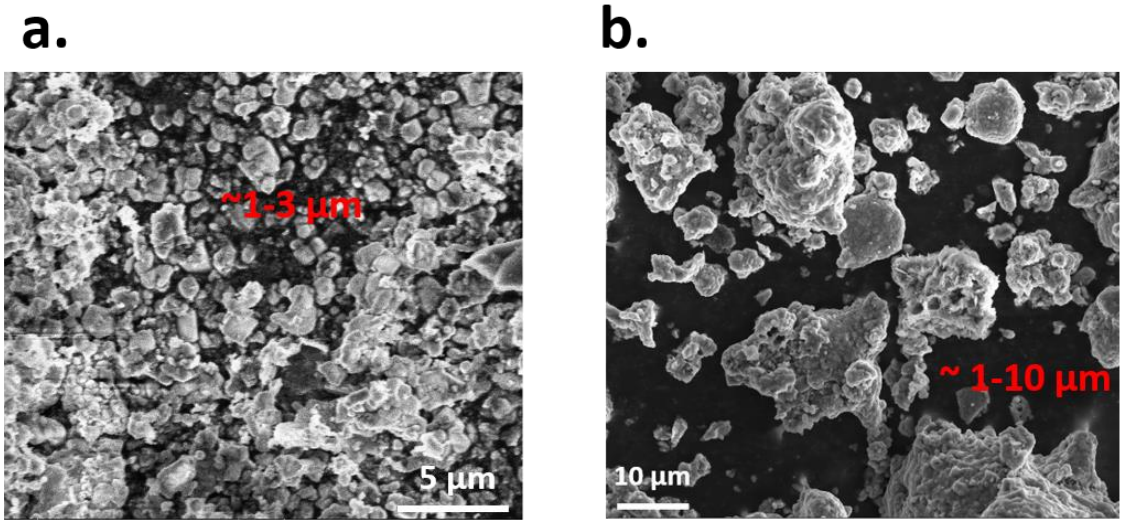

Figure S7. SEM images of NVPF (**a**) and NVP (**b**) powders. The particle size is indicated on each image.

Part V. Diffusion coefficient estimation using PITT and Randles-Sevcik

i. Potentiostatic Intermittent Titration Technique (PITT)

The PITT procedure is based on a staircase potential signal applied to the system, as represented in **Figure S4a**. In the case of a planar electrode, Montella demonstrated that the current response of the system is dictated by the well-known Cottrell relationship for short times and an exponential decay of diffusion current with respect to time for long times, if a restricted diffusion condition and diffusion control (very fast insertion reaction kinetics) are assumed.[3]

For short times, *i.e.* $t \ll \frac{L^2}{\pi^2 D_{app}}$,

$$I_d(t)_{st} = I_{cottrell}(t) = -\frac{FA\sqrt{D_{app}'}\Delta c}{\sqrt{\pi t}} \qquad \textbf{Equation S1}$$

For long times, *i.e.* $t \gg \frac{L^2}{\pi^2 D_{app}}$,

$$I_d(t)_{st} = I_{cottrell}(t) = 2FA\frac{D_{app}}{L}\Delta c\ exp\left(-\frac{\pi^2 D_{app}}{4L^2}t\right) \qquad \textbf{Equation S2}$$

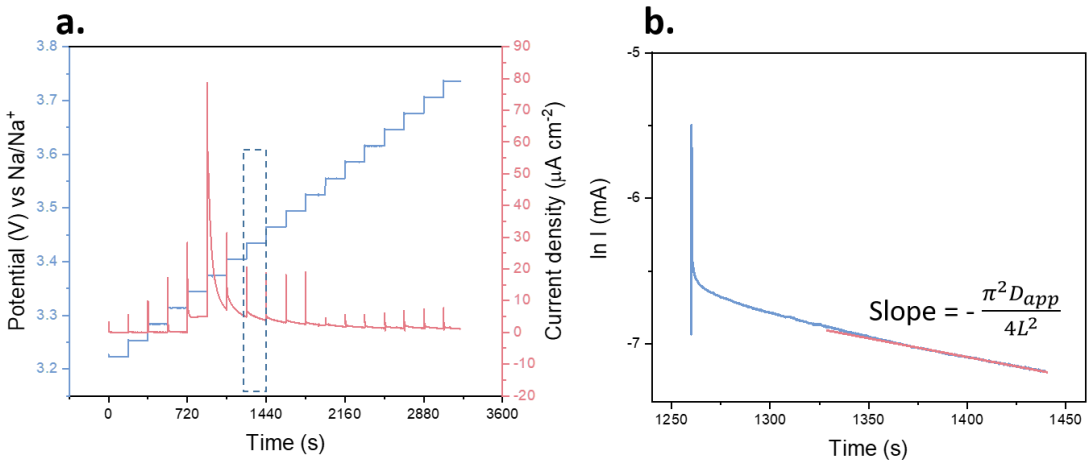

Figure S8. (a) Applied potential staircases and current response of the NVP system in a 1M $NaPF_6$ in EC:DMC 1%*vol* electrolyte. Focus on **(b)** the natural logarithm of the current response for the 3.47 V vs. Na/Na^+ staircase.

where F is the Faraday's constant (96485 $C.mol^{-1}$), A is the specific surface are (0.196 cm^2), Δc is the concentration variation in the film ($mol.cm^{-3}$), L is the film thickness (cm) and D_{app}' is the apparent diffusion coefficient in the solid phase ($cm^2.s^{-1}$). Then, the apparent diffusion coefficient can be extracted from slope of the natural logarithm of the **Equation S2** (**Figure S7b**), as it is independent of unknown variables.

ii. Randles-Sevcik Equation

Randles-Sevcik equation was employed to estimate the apparent diffusion coefficient of Na^+ into NVP and NVPF frameworks. Cyclic voltammetry measurements at multiple rates were performed (**Figure S8**), then, assuming a Nernstian redox reaction (*i.e.* a fast reversible electron transfer reaction), the absolute current peak value has a linear relationship (in oxidation and reduction) to the square root of the scan rate of the cyclic voltammetry, following this equation[4]:

$$I_p = 0.4463\, FS \sqrt{\frac{F}{RT}} \frac{S_e}{S} \sqrt{D_{app} x}\, C_{mat} \nu^{1/2} \qquad \textbf{Equation S3}$$

where F is the Faraday's constant (96485 $C.mol^{-1}$), R is the gas constant ($J.K^{-1}.mol^{-1}$), T is the temperature (K), Se and S are the specific surface and geometric area, respectively (cm^2), x is the maximal mole fraction of inserted cation that can be inserted in the host material, C_{mat} is the concentration of Na^+ cation in the host material ($mol.cm^{-3}$) (0.0077 mol cm^{-3} for NVPF and 0.0069 mol cm^{-3} for NVP, respectively)[5], ν is the scan rate ($V.s^{-1}$), I_p is the value of the current peak (A) and D_{app} is the apparent diffusion coefficient of the inserted cation in the solid phase ($cm^2.s^{-1}$).

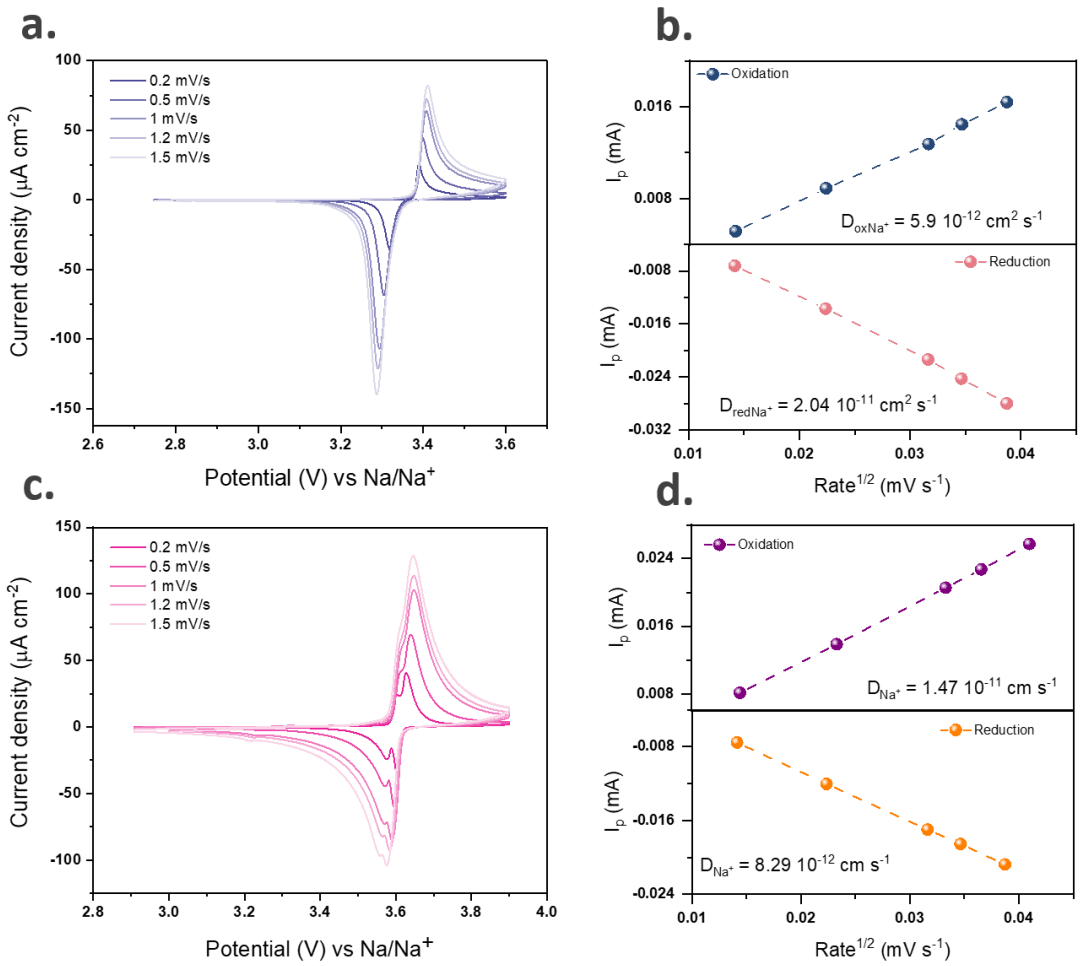

Figure S9. CV profiles at different scan rates (0.2 to 1.5 mV s^{-1}) of NVP **(a)** and NVPF **(c)** cycled in 1M $NaPF_6$ in EC:DMC 1%*vol* electrolyte. Apparent Na^+ diffusion coefficient of NVP **(b)** and NVPF **(d)** calculated from **Equation S3** during oxidation (top) and reduction (bottom).

Part VI. MD simulations

Molecular dynamics simulations were performed in the LAMMPS program.[6] Initial configurations and input files were generated using Packmol,[7] VESTA[8] and fftool.[9] The simulation box consisted of two electrodes, NVP and gold ones, separated by the $NaPF_6$/PC solution. The NVP electrode was represented by rhombohedral R-3c space group[10] with the [001] plane exposed towards the solvent, following the recommendations from the literature.[11] The gold electrode was represented by cubic Fm-3m space group[12] with the [100] plane exposed to the solvent. The liquid phase contained 75 ion pairs of $NaPF_6$ salt and 830 molecules of PC, matching the experimental composition. The total system size was approximately 15 000 atoms.

The Na^+ cation were represented using Aqvist force field,[13] while the parameters of PF_6^- were taken from the CL&P model.[14] The intermolecular interaction parameters of the NVP and gold electrodes, given in **Table S1**, were considered from several sources.[13,15–17] The bonded and non-bonded parameters of PC were taken from the OPLS-AA,[18] except for the partial charges, which were computed using the CHelpG procedure[19] on electron densities obtained at the MP2/cc-pVTZ level of theory at previously optimized geometries with the Gaussian16 program.[20] The PC model was validated by computing density and viscosity of bulk liquid $NaPF_6$/PC system.

Table S1. Non-bonded Lennard-Jones interaction parameters of NVP and Au electrodes.

Atom	q / e^-	σ / Å	ε / kJ mol^{-1}	Ref.
Na	+1	3.330	0.0120	[13]
V	+3	2.673	0.0602	[15]
P	+5	3.740	0.1400	[16]
O	-2	3.150	0.1700	[16]
Au	0	2.951	22.1334	[17]

The system had a total size of 34.92×30.24×160.0 Å, with the thickness of ~20 Å and ~12 Å for the NVP and Au electrodes, respectively. The simulation box was periodic in *x* and *y* direction, and a slab of $3\times l_z$ was added along the *z* direction. A cutoff of 12 Å was considered for non-bonded interactions. The particle-particle particle-mash (PPPM) method was used to evaluate electrostatic energies (the accuracy of $1\cdot10^{-5}$), with the slab correction applied. Both electrodes were considered immobile. Bonds terminating with hydrogen atoms were constrained using the SHAKE algorithm. The time step was set to 1 fs. The Nosé-Hoover thermostat was used to keep the temperature of the electrolyte solution at 298 K. The system was equilibrated for 5 ns in the NVT ensemble.

The radial distribution functions around Na^+ ions and the density profiles along the *z* direction were obtained from the 50 ns trajectory, which followed the equilibration step. The coordination number plots were obtained from a separate production run, during which a single Na^+ ion was pulled from the solution towards the NVP surface. For this, the Na^+ atom was tethered by a harmonic spring of 125 kcal mol^{-1} $Å^{-1}$ and moved from 10.0 Å to 2.0 Å (with the respect to the top Na layer of the NVP electrode) with a step of 0.25 Å. At each step, the system was equilibrated for 100 ps and the coordination number was recorded during following 200 ps. The coordination number cutoff was set to 4.55 Å for P of PF_6^- and 3.20 Å for O atoms of the the carbonyl group of PC, being defined as the position of the first minimum of the corresponding radial distribution functions (**Figure S9**). The data analysis was performed using TRAVIS[21] and our self-written tools. The visualization of the simulation box was done in VMD.[22]

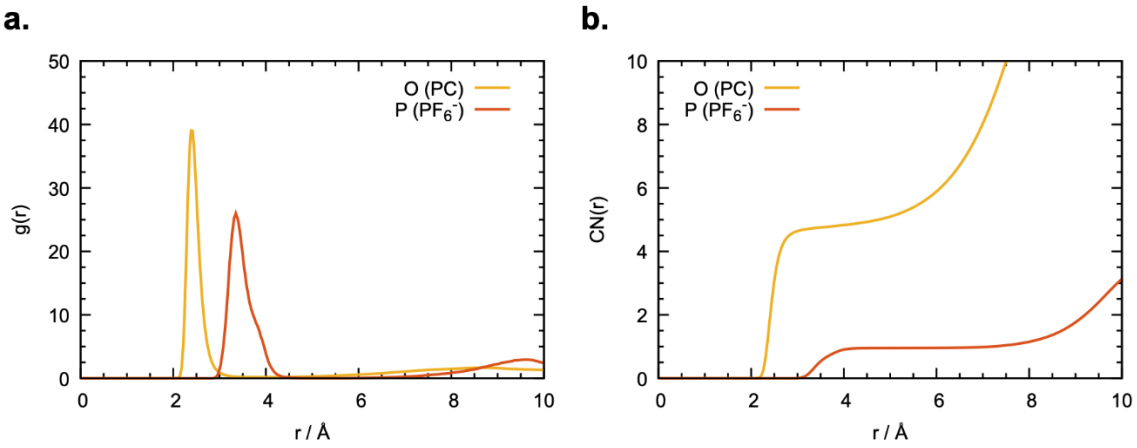

Figure S10. Radial distribution functions (**a**) and coordination numbers (**b**) of P of PF_6^- and O atoms of the carbonyl group of PC around the Na^+ ion.

References

[1] P. Lemaire, T. Dargon, D. Alves Dalla Corte, O. Sel, H. Perrot, J.-M. Tarascon, Anal. Chem. 2020, 92, 13803.

[2] R. Dugas, A. Ponrouch, G. Gachot, R. David, M. R. Palacin, J. M. Tarascon, J. Electrochem. Soc. 2016, 163, A2333.

[3] C. Montella, J. Electroanal. Chem. 2002, 518, 61.

[4] J. J. V. Benschoten, J. Y. Lewis, W. R. Heineman, D. A. Roston, P. T. Kissinger, Cyclic voltammetry experiment, Division of Chemical Education, 1983.

[5] Z. Yang, G. Li, J. Sun, L. Xie, Y. Jiang, Y. Huang, S. Chen, Energy Storage Mater. 2020, 25, 724.

[6] S. Plimpton, J. Comput. Phys. 1995, 117, 1.

[7] L. Martínez, R. Andrade, E. G. Birgin, J. M. Martínez, J. Comput. Chem. 2009, 30, 2157.

[8] K. Momma, F. Izumi, J. Appl. Crystallogr. 2011, 44, 1272.

[9] A. Padua, fftool.

[10] I. V. Zatovsky, Acta Crystallogr. Sect. E Struct. Rep. Online 2010, 66, i12.

[11] J.-N. Chotard, G. Rousse, R. David, O. Mentré, M. Courty, C. Masquelier, Chem. Mater. 2015, 27, 5982.

[12] I.-K. Suh, H. Ohta, Y. Waseda, J. Mater. Sci. 1988, 23, 757.

[13] J. Åqvist, J. Phys. Chem. 1990, 94, 8021.

[14] J. N. Canongia Lopes, J. Deschamps, A. A. H. Pádua, J. Phys. Chem. B 2004, 108, 2038.

[15] S. Gupta, N. Wai, T. M. Lim, S. H. Mushrif, J. Mol. Liq. 2016, 215, 596.

[16] K. Murzyn, M. Bratek, M. Pasenkiewicz-Gierula, J. Phys. Chem. B 2013, 117, 16388.

[17] H. Heinz, R. A. Vaia, B. L. Farmer, R. R. Naik, J. Phys. Chem. C 2008, 112, 17281.

[18] W. L. Jorgensen, D. S. Maxwell, J. Tirado-Rives, J. Am. Chem. Soc. 1996, 118, 11225.

[19] C. M. Breneman, K. B. Wiberg, J. Comput. Chem. 1990, 11, 361.

[20] M. J. Frisch, G. W. Trucks, H. B. Schlegel, G. E. Scuseria, M. A. Robb, J. R. Cheeseman, G. Scalmani, V. Barone, G. A. Petersson, H. Nakatsuji, X. Li, M. Caricato, A. V. Marenich, J. Bloino, B. G. Janesko, R. Gomperts, B. Mennucci, H. P. Hratchian, J. V. Ortiz, A. F. Izmaylov, J. L. Sonnenberg, Williams, F. Ding, F. Lipparini, F. Egidi, J. Goings, B. Peng, A. Petrone, T. Henderson, D. Ranasinghe, V. G. Zakrzewski, J. Gao, N. Rega, G. Zheng, W. Liang, M. Hada, M. Ehara, K. Toyota, R. Fukuda, J. Hasegawa, M. Ishida, T. Nakajima, Y. Honda, O. Kitao, H. Nakai, T. Vreven, K. Throssell, J. A. Montgomery Jr., J. E. Peralta, F. Ogliaro, M. J. Bearpark, J. J. Heyd, E. N. Brothers, K. N. Kudin, V. N. Staroverov, T. A. Keith, R. Kobayashi, J. Normand, K. Raghavachari, A. P. Rendell, J. C. Burant, S. S. Iyengar, J. Tomasi, M. Cossi, J. M. Millam, M. Klene, C. Adamo, R. Cammi, J. W. Ochterski, R. L. Martin, K. Morokuma, O. Farkas, J. B. Foresman, D. J. Fox, Gaussian 16 Rev. C.01, Wallingford, CT, 2016.

[21] M. Brehm, B. Kirchner, J. Chem. Inf. Model. 2011, 51, 2007.

[22] W. Humphrey, A. Dalke, K. Schulten, J. Mol. Graph. 1996, 14, 33.